1

Interpretability Meets Accuracy in Computational Spectroscopy: The Virtual Multifrequency Spectrometer

Vincenzo Barone[1] *and Cristina Puzzarini*[2]

[1] *Scuola Normale Superiore, Piazza dei Cavalieri 7, 56126 Pisa, Italy*
[2] *Università di Bologna, Dipartimento di Chimica "Giacomo Ciamician", Via Selmi 2, 40126 Bologna, Italy*

The virtual multifrequency spectrometer (VMS), under active development in our laboratories over the last few years, is shortly described in this chapter by means of selected spectroscopic techniques and a few representative case studies. The VMS project aims to offer an answer to the following question: is it possible to turn strongly specialized research in the field of computational spectroscopy into robust and user-friendly aids to experiments and industrial applications? VMS contains a number of tools devised to increase the interaction between researchers with different background and to push toward new frontiers in computational chemistry. As a matter of fact, the terrific advancements in computational spectroscopy and the wide availability of computational and analytic tools are paving the route toward the study of problems that were previously too difficult or impossible to be solved and let imagine even more ambitious targets for fundamental and applied research. Under such circumstances, a robust, flexible, and user-friendly tool can allow for moving data analysis toward a proactive process of strategic decisions and actions. This chapter starts from these premises, and it proposes a perspective for a new virtual platform aimed at integrating past developments in theory, algorithms, and software with new workflow management and visualization tools. After a short review of the underlying theoretical framework, the features of the principal tools available in the current version of VMS for a selection of spectroscopic techniques are addressed in some details. Next, four case studies are presented, thus aiming to illustrate possible applications of VMS to systems of current interest for both fundamental and applied research. These applications convincingly show that even if several extensions of the software are planned or already under development, VMS represents a powerful and user-friendly tool for both computational and experimentally oriented spectroscopists.

Molecular Spectroscopy: A Quantum Chemistry Approach,
First Edition. Edited by Yukihiro Ozaki, Marek Janusz Wójcik, and Jürgen Popp.

1.1 Introduction

Spectroscopic techniques provide a wealth of qualitative and quantitative information on the chemical and physical–chemical properties of molecular systems in a variety of environments. Nowadays, sophisticated experimental techniques, mainly based on vibrational, electronic, and resonance spectroscopies, allow studies under various environmental conditions and in a noninvasive fashion [1, 2]. Particularly effective strategies are obtained when different spectroscopic techniques are combined together and further supported and/or integrated by computational approaches. Indeed, not only the spectral analysis is seldom straightforward, but also molecular spectra do not provide direct information on molecular structures, properties, and dynamics [3, 4]. The challenges can be posed by the intrinsic properties and complexity of the system and/or caused by thermal or environmental effects, whose specific roles are not easy to separate and evaluate. In such a context, computational spectroscopy is undoubtedly a powerful and reliable tool to unravel the different contributions to the spectroscopic signal and understand the underlying physical phenomena [5, 6]. However, direct vis-à-vis comparisons between experimental and computed spectroscopic data are still far from being standard. To fill this lack, a virtual multifrequency spectrometer (VMS) (http://dreamslab.sns.it/vms/) has been implemented with the aim of providing a user-friendly access to the latest developments of computational spectroscopy, also to nonspecialists [7–11]. As it will be better explained in the following section, VMS integrates state-of-the-art computational implementations of different spectroscopies with a powerful graphical user interface (GUI) [12], which offers an invaluable aid in preorganizing and displaying the computed spectroscopic information. For the sake of clarity, it should be noted that several codes incorporate implementation of spectroscopic properties at different levels of theory together with graphic engines. However, none of these tools offer the characteristics that should be considered mandatory for state-of-the-art computational spectroscopy (e.g. rigorous treatment of anharmonicity, vibronic contributions, etc.) and/or for flexible user-friendly graphical tools. In particular, it should emphasize the uniqueness of VMS in incorporating both general utilities needed by experimentally oriented scientists (e.g. conversion of theoretical quantities to experimental observables, manipulation of several spectra at the same time, etc.) and advanced tools for theoreticians and developers (e.g. resonance Raman [RR] spectra).

The aim of the present chapter is to provide an overview of the VMS software, thus focusing on its peculiarities and unique features. The chapter is organized as follows. In the following section, a brief summary of the general machinery of the VMS program and of the main technical aspects will be provided. This will be followed by a short introduction of the theoretical background for the selected spectroscopies (e.g. rotational, vibrational, vibronic, and magnetic) and of the corresponding quantum chemical (QC) requirements. Then, the current status of VMS will be presented in some detail with specific reference to rotational, vibrational, vibronic, and magnetic spectroscopy. Finally, applications will be illustrated with the help of four case studies, which will allow the capabilities of VMS to be demonstrated. Some general considerations will conclude the chapter.

1.2 The Virtual Multifrequency Spectrometer

VMS is a tool that integrates a wide range of computational and experimental spectroscopic techniques and aims at predicting and analyzing different types of molecular spectra as well as disclosing the static and dynamic physical–chemical information they contain [7]. VMS is mainly composed of two parts, namely, VMS-Comp, which provides access to the latest developments in the field of computational spectroscopy, and VMS-Draw, which provides a powerful GUI for an intuitive interpretation of theoretical outcomes and a direct prediction or comparison to experiment (http://dreamslab.sns.it/vms/) [7].

The spectroscopies supported by VMS are electron spin resonance (ESR), nuclear magnetic resonance (NMR), rotational (microwave [MW]), infrared (IR), vibrational circular dichroism (VCD), nonresonant Raman (nRR), resonance Raman, Raman optical activity (ROA), resonance Raman optical activity (RROA), electronic one-photon absorption (OPA) (i.e. UV–vis) and one-photon emission (OPE) (i.e. fluorescence), electronic circular dichroism (ECD), and circularly polarized luminescence (CPL).

1.2.1 The VMS Framework

The framework of the VMS program is graphically shown in Figure 1.1 [7]. The key feature of VMS is to provide a user-friendly access to computational spectroscopy tools also to nonspecialists. VMS integrates a powerful GUI, VMS-Draw, which offers an invaluable aid in the pre- and post-processing stages [12]. This permits a direct way to present the information produced by *in vitro* and *in silico* experiments, thus allowing the user to focus the attention on the underlying physical–chemical features without being concerned with technical details. VMS-Draw is interfaced with VMS-Comp [8, 9, 13], which

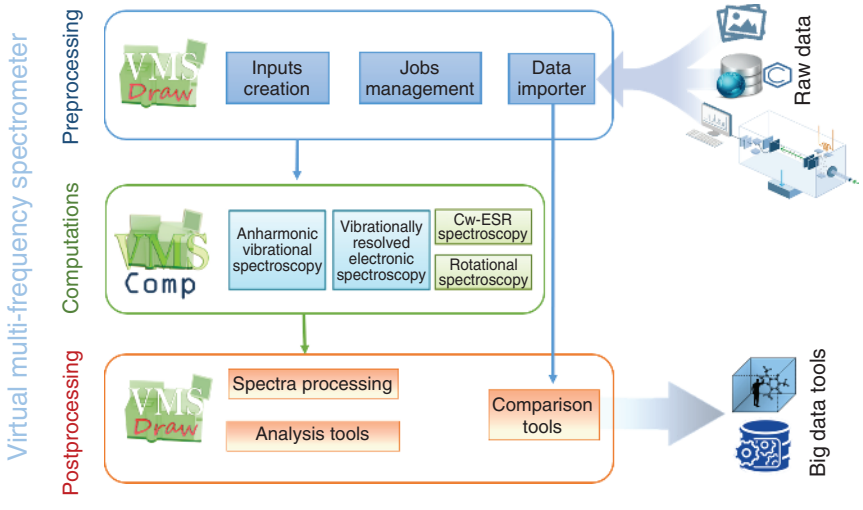

Figure 1.1 The framework of the virtual multifrequency spectrometer.

takes care of QC computations of the required spectroscopic parameters and all high-performance computing (HPC) aspects [7, 12]. Both VMS-Draw and VMS-Comp modules are either fully embedded with the Gaussian package [14] or loosely bound to other suites of QC programs, such as CFOUR [15]. In the last case, general input–output facilities as well as *ad hoc* scripts that permit effective interactions with other electronic structure codes than Gaussian have been developed or are still under development (see, for example, Ref. [10]). Overall, VMS has access to almost all computational models and to properties that are not yet available in the reference QC Gaussian suite. In addition to the large availability of QC methods and properties, VMS has the unique feature of allowing state-of-the-art computational spectroscopy studies driven by a flexible user-friendly graphical tool that furthermore includes those general utilities needed by experimentally oriented scientists (e.g. manipulations of several spectra at the same time, spectral normalization, etc.) and advanced tools for theoreticians and developers (e.g. resonance Raman spectroscopy). In the following sections, the theoretical background and the QC requirements for quantitative spectral prediction/analysis of selected spectroscopies are presented together with a description of the spectral simulation facilities and of the corresponding results.

1.2.2 The VMS Framework: Spectroscopies and Theoretical Background

The complete list of the spectroscopies available within the VMS software has been given above. In this chapter, we limit ourselves to the discussion of a selection of spectroscopies, namely, the rotational, vibrational, vibronic, and magnetic spectroscopies, for which we provide a short description of the theoretical background.

1.2.2.1 Rotational Spectroscopy

The terms of the effective rotational Hamiltonian are the pure rotational and centrifugal distortion contributions, which describe the rotational energy levels for a given vibrational state, with the ground state usually being the one of interest. While a complete treatment can be found in the literature (see, for example, Ref. [16]), here, we recall just the key aspects of interest.

The basic rotational Hamiltonian, within the semirigid rotor approximation, can be written as

$$H_{\mathrm{rot}} = H_{\mathrm{R}} + H_{\mathrm{qcd}} + H_{\mathrm{scd}} + \cdots \tag{1.1}$$

where H_{qcd} and H_{scd} are the quartic and sextic centrifugal terms, respectively. The dots refer to the possibility of including higher-order centrifugal contributions. H_{R} is the rigid rotor Hamiltonian:

$$H_{\mathrm{R}} = \sum_{\tau} \mathrm{B}_{\tau}^{\mathrm{eq}} \mathrm{J}_{\tau}^{2} \tag{1.2}$$

where $\mathrm{B}_{\tau}^{\mathrm{eq}}$ has been defined as follows:

$$\mathrm{B}_{\tau}^{\mathrm{eq}} = \frac{\hbar^2}{2hcI_{\tau\tau}^{\mathrm{eq}}} \tag{1.3}$$

where τ refers to the inertial axis. From a computational point of view, the equilibrium rotational constants are straightforwardly obtained from the geometry optimization.

Even if the equilibrium contribution to rotational constants is the most important, the effect of molecular vibrations cannot be neglected when aiming at a quantitative description of rotational spectra. Therefore, the term describing the dependence of the rotational constants on the vibrational quantum numbers should be incorporated in Eq. (1.3), and equilibrium rotational constants should be replaced by the effective rotational constants that contain the contributions beyond the rigid rotor harmonic oscillator (RRHO) approximation. Their effects on rotational motion can be conveniently described by means of vibrational perturbation theory (VPT), and we refer the reader to, for example, Refs. [16, 17] for a detailed treatment. While there are no corrections at the first order in VPT, at the second order (VPT2), the expression becomes [18]:

$$\mathrm{B}_{\tau}^{\mathrm{v}} = \mathrm{B}_{\tau}^{\mathrm{eq}} - \sum_{i=1}^{N} \alpha_{i,\tau} \left(v_i + \frac{d_i}{2} \right) \tag{1.4}$$

where the superscript v denotes a specific vibrational state and the sum runs on all fundamental vibrational modes i, with v_i being the corresponding quantum number and d_i its degeneracy order. The $\alpha_{i,\tau}$ values are the so-called vibration–rotation interaction constants and contain three contributions: the first one is a corrective term related to the moment of inertia, the second one is due to the Coriolis interactions, and the last is an anharmonic correction. Therefore, from a computational point of view, anharmonic force field (FF) calculations are required to correct the equilibrium rotational constants for vibrational effects.

The quartic centrifugal distortion Hamiltonian is defined as

$$H_{\mathrm{qcd}} = \frac{1}{4} \sum_{\tau\eta\varsigma\varrho} \tau_{\tau\eta\varsigma\varrho} \mathbf{J}_{\tau} \mathbf{J}_{\eta} \mathbf{J}_{\varsigma} \mathbf{J}_{\varrho} \tag{1.5}$$

where the tensor $\tau_{\tau\eta\varsigma\varrho}$ depends only on the harmonic part of the potential energy surface (PES). To obtain the quartic centrifugal distortion parameters actually employed, further contact transformations with purely rotational operators (thus diagonal in the vibrational quantum numbers) are then required. An analogous expression can be written for the sextic centrifugal distortion term H_{scd}, and the computation of the corresponding sextic centrifugal distortion constants involves harmonic, anharmonic, and Coriolis perturbation terms. Therefore, from a computational point of view, anharmonic force field computations are needed for their determination. To relate the experimental parameters to combinations of $\tau_{\tau\eta\varsigma\varrho}$ ($\tau_{\tau\eta\varsigma\varrho\epsilon\iota}$ in the case of sextics), it is necessary to further completely reduce the Hamiltonian. Different results are then obtained depending on the reduction chosen; see, for example, Refs. [16, 17, 19].

1.2.2.2 Vibrational Spectroscopy

For the simulation of vibrational spectra, a purely vibrational Hamiltonian (H_{vib}) is commonly used. In the framework of VPT2, which is based on Taylor expansions of the harmonic potential (V), vibrational (E_{v}) energies, and vibrational

wavefunction, up to the second order [20], the vibrational Hamiltonian is defined as follows:

$$H_{\text{vib}} = \frac{1}{2}\sum_{i=1}^{N}\omega_i(\mathbf{p}_i{}^2 + \mathbf{q}_i{}^2) + \frac{1}{6}\sum_{i,j,k=1}^{N} k_{ijk}\mathbf{q}_i\mathbf{q}_j\mathbf{q}_k + \frac{1}{24}\sum_{i,j,k,l=1}^{N} k_{ijkl}\mathbf{q}_i\mathbf{q}_j\mathbf{q}_k\mathbf{q}_l + \sum_{\tau}\mathrm{B}_{\tau}^{\text{eq}}\sum_{i,j,k,l=1}^{N}\zeta_{ij,\tau}\zeta_{kl,\tau}\sqrt{\frac{\omega_i\omega_k}{\omega_j\omega_l}}\mathbf{q}_i\mathbf{p}_j\mathbf{q}_k\mathbf{p}_l + U \tag{1.6}$$

For asymmetric tops, at the VPT2 level, the energy (E_m, in cm^{-1}) of a given vibrational state m is given by

$$E_m = E_0 + \sum_{i=1}^{N} v_i^m\omega_i + \sum_{i,j=1}^{N}\chi_{ij}\left[v_i^m v_j^m + \frac{1}{2}(v_i^m + v_j^m)\right] \tag{1.7}$$

where v_i^m is the number of quanta associated with mode i in state m and ω_i the corresponding harmonic wavenumber. E_0 is the zero-point vibrational energy, which is defined as follows:

$$E_0 = \sum_{i=1}^{N}\frac{\omega_i}{2} + \sum_{i,j=1}^{N}\frac{k_{iijj}}{32} - \sum_{i,j,k=1}^{N}\left[\frac{k_{iik}k_{jjk}}{32\omega_k} + \frac{k_{ijk}{}^2}{48(\omega_i+\omega_j+\omega_k)}\right] - \sum_{\tau}\frac{\mathrm{B}_{\tau}^{\text{eq}}}{4}\left[1 - \sum_{i=1}^{N-1}\sum_{j=i+1}^{N}\{\zeta_{ij,\tau}\}^2\frac{(\omega_i-\omega_j)^2}{\omega_i\omega_j}\right] \tag{1.8}$$

In Eq. (1.7), χ is the anharmonicity contributions matrix, with its elements given by

$$16\chi_{ii} = k_{iiii} - \frac{5k_{iii}{}^2}{3\omega_i} - \sum_{\substack{j=1\\ j\neq i}}^{N}\frac{(8\omega_i{}^2 - 3\omega_j{}^2)k_{iij}{}^2}{\omega_j(4\omega_i{}^2 - \omega_j{}^2)} \tag{1.9}$$

$$4\chi_{ij} = k_{iijj} - \frac{2\omega_i k_{iij}{}^2}{(4\omega_i{}^2 - \omega_j{}^2)} - \frac{2\omega_j k_{ijj}{}^2}{(4\omega_j{}^2 - \omega_i{}^2)} - \frac{k_{iii}k_{ijj}}{\omega_i} - \frac{k_{jjj}k_{iij}}{\omega_j} + \sum_{\substack{k=1\\ k\neq i,j}}^{N}\left[\frac{2\omega_k(\omega_i{}^2 + \omega_j{}^2 - \omega_k{}^2)k_{ijk}{}^2}{\Delta_{ijk}} - \frac{k_{iik}k_{jjk}}{\omega_k}\right] + \frac{4(\omega_i{}^2 + \omega_j{}^2)}{\omega_i\omega_j}\sum_{\tau}\mathbf{B}_{\tau}^{\text{eq}}\{\zeta_{ij,\tau}\}^2 \tag{1.10}$$

where

$$\Delta_{ijk} = \omega_i{}^4 + \omega_j{}^4 + \omega_k{}^4 - 2(\omega_i{}^2\omega_j{}^2 + \omega_i{}^2\omega_k{}^2 + \omega_j{}^2\omega_k{}^2) \tag{1.11}$$

Transition energies from the ground state ν_m are therefore straightforwardly obtained from Eqs. (1.7) and (1.8) as $E_m - E_0$ difference.

The intensities for a broad range of spectroscopies at the VPT2 level can be obtained by referring to a generic property $\mathbf{P}$, which can depend on either the normal coordinates ($\mathbf{q}$) or their conjugate momenta ($\mathbf{p}$):

$$\mathbf{P} = \mathbf{P}^{(0)} + \mathbf{P}^{(1)} + \mathbf{P}^{(2)} \tag{1.12}$$

where

$$\mathbf{P}^{(0)} = \mathbf{P}^{\mathrm{eq}} + s_0 \sum_{i=1}^{N} \mathbf{P}_i (a_i^{\dagger} + S a_i) \tag{1.13}$$

$$\mathbf{P}^{(1)} = s_1 \sum_{i=1}^{N} \sum_{j=1}^{N} \mathbf{P}_{ij} q_j (a_i^{\dagger} + S a_i) \tag{1.14}$$

$$\mathbf{P}^{(2)} = s_2 \sum_{i=1}^{N} \sum_{k=1}^{N} \sum_{j=1}^{N} \mathbf{P}_{ijk} q_j q_k (a_i^{\dagger} + S a_i) \tag{1.15}$$

In equations above, $a_i^{\dagger}$ and a_i are the creation and annihilation operators, respectively; s_0, s_1, and s_2 are constant factors; and S corresponds to a sign (i.e. it represents the multiplication by +1 or −1). The function of Eq. (1.12) is then used to obtain analytic formulas for the transition moments up to three quanta [21–25] and can be simply related to the property of interest by identifying the variables in Eqs. (1.12)–(1.15) with the actual quantities, as exemplified in Figure 1.2. The electric ($\boldsymbol{\mu}$) and magnetic ($\mathbf{m}$) dipoles and the polarizability ($\boldsymbol{\alpha}$) are used in IR, VCD, and Raman intensities, respectively, whereas the electric dipole–magnetic dipole optical activity ($\mathbf{G'}$) and the electric dipole–electric quadrupole ($\mathbf{A}$) tensors also enter the ROA intensities [13].

From a quick inspection of Eqs. (1.9) and (1.10), it is evident that for the VPT2 energies, the denominator might become exceedingly small. This situation leads to the so-called Fermi resonances (FRs), which can be distinguished in type I ($\omega_i \approx 2\omega_j$) and type II ($\omega_i \approx \omega_j + \omega_k$). Indeed, a near resonance can be sufficient to obtain unphysical results due to an excessive contribution from anharmonicity. This is a well-known issue of VPT2, which has been extensively studied in the literature [16, 26–39] and needs to be correctly addressed for a successful application of this method. A major difficulty lies in the definition of the resonance conditions. In the literature, several efficient identification processes have been

$\mathbf{P}$	$\mathbf{P}_0$	$\mathbf{P}_i$	$\mathbf{P}_{ji}$	$\mathbf{P}_{jki}$	s_0	s_1	s_2	S
$\boldsymbol{\mu}$	$\boldsymbol{\mu}^{\mathrm{eq}}$	$\frac{\partial \boldsymbol{\mu}}{\partial q_i}$	$\frac{\partial^2 \boldsymbol{\mu}}{\partial q_i q_j}$	$\frac{\partial^3 \boldsymbol{\mu}}{\partial q_i q_j q_k}$	$\frac{1}{\sqrt{2}}$	$\frac{1}{2\sqrt{2}}$	$\frac{1}{6\sqrt{2}}$	+1
$\mathbf{m}$	$\mathbf{0}$	$\mathbf{M}_i$	$\frac{\partial \mathbf{M}}{\partial q_i}$	$\frac{\partial^2 \mathbf{M}}{\partial q_i q_j}$	$\frac{i\hbar}{\sqrt{2}}$	$\frac{i\hbar}{\sqrt{2}}$	$\frac{i\hbar}{2\sqrt{2}}$	−1
$\boldsymbol{\alpha}$	$\boldsymbol{\alpha}^{\mathrm{eq}}$	$\frac{\partial \boldsymbol{\alpha}}{\partial q_i}$	$\frac{\partial^2 \boldsymbol{\alpha}}{\partial q_i q_j}$	$\frac{\partial^3 \boldsymbol{\alpha}}{\partial q_i q_j q_k}$	$\frac{1}{\sqrt{2}}$	$\frac{1}{2\sqrt{2}}$	$\frac{1}{6\sqrt{2}}$	+1
$\mathbf{G'}$	$\mathbf{G'}^{\mathrm{eq}}$	$\frac{\partial \mathbf{G'}}{\partial q_i}$	$\frac{\partial^2 \mathbf{G'}}{\partial q_i q_j}$	$\frac{\partial^3 \mathbf{G'}}{\partial q_i q_j q_k}$	$\frac{1}{\sqrt{2}}$	$\frac{1}{2\sqrt{2}}$	$\frac{1}{6\sqrt{2}}$	+1
$\mathbf{A}$	$\mathbf{A}^{\mathrm{eq}}$	$\frac{\partial \mathbf{A}}{\partial q_i}$	$\frac{\partial^2 \mathbf{A}}{\partial q_i q_j}$	$\frac{\partial^3 \mathbf{A}}{\partial q_i q_j q_k}$	$\frac{1}{\sqrt{2}}$	$\frac{1}{2\sqrt{2}}$	$\frac{1}{6\sqrt{2}}$	+1

Figure 1.2 Equivalence relations between the model property **P** and actual properties.

presented [26, 28–30, 33, 36–40]. Then, those terms that have been identified as resonant should be removed from the perturbative treatment for the calculation of the energy. This approach is named deperturbed VPT2 (DVPT2). To take into account the missing terms, an *ad hoc* variational step, which reintroduces the previously discarded terms, can be performed using the DVPT2 vibrational energies as references. We refer to the overall resulting procedure as generalized VPT2 (GVPT2). An alternative approach has been proposed by Kuhler, Truhlar, and Isaacson and denoted degeneracy-corrected PT2 (DCPT2); this is based on replacing the potentially resonant terms with nonresonant forms derived from a model system considering only the two states involved [29]. A shortcoming of this approach is a potential inaccuracy for each replaced terms far from resonance; this can be partially corrected by introducing a switch function that will mix the DCPT2 and VPT2 results for each potentially resonant term, thus leading to the so-called hybrid DCPT2-VPT2 (HDCPT2) [37]. Finally, other types of resonance should be mentioned; these are collectively denoted as Darling–Dennison resonances (DDRs) [26, 30, 32, 39–45] and are commonly treated through a variational procedure, analogous to that used for FRs. In the following, we always refer to GVPT2, and this includes corrections to both Fermi and DDRs.

The problem of resonances in intensity calculations has been more scarcely addressed in the literature, and limited is the number of programs supporting them [13, 23, 27, 39, 44]. Since they are related to the mechanical anharmonicity (wavefunction), it is possible to use the analysis for the energy shortly addressed above also for the transition moments. However, an important difference is the impact of DDRs, which can lead to incorrect intensities. Depending on the protocol applied for the definition of DDRs, it may be necessary to complement it with an *ad hoc* test targeted to handle the most critical cases (for instance, of near-equal energies) [13, 46]. The eigenvectors ($\mathbf{L}_\mathrm{E}$) of the matrix diagonalized to introduce the variational contribution of resonances to energies are used to project the deperturbed transition moments on the variationally corrected states following the procedure described in Ref. [23]:

$$\langle \mathbf{P} \rangle_{I,\mathrm{F}}^{\mathrm{var}} = \mathbf{L}_\mathrm{E}^\mathrm{T} \langle \mathbf{P} \rangle_{I,\mathrm{F}}^{\mathrm{VPT2}} \tag{1.16}$$

In the VMS framework, all the required strategies for a correct derivation of the intensities are implemented.

1.2.2.3 Vibronic Spectroscopy

A reliable description of molecular vibrations in ground and excited electronic states is at the heart of an accurate simulation of vibrational modulation (hereafter vibronic in a broad sense) effects in UV–vis spectra and their chiroptical (e.g. ECD) counterparts. Indeed, experimental spectra originate from the convolution of vibronic transitions, thus usually leading to highly asymmetric band-shaped spectra at both low and high resolution. From a theoretical point of view, a rigorous inclusion of rovibrational effects beyond the standard rigid rotor harmonic oscillator approximation can be performed for small molecules, whereas for larger systems, feasible approaches are currently based on neglecting the rovibrational coupling and on the Franck–Condon (FC) principle at the harmonic level. Within this framework, a general sum-over-state expression

for the vibronic contributions to the transition between two electronic states has been derived for OPA, OPE, ECD, and CPL [47, 48], and it has been recently extended to resonance Raman, its chiroptical counterpart RROA, and also spin-forbidden transitions [49], with the corresponding intensity being expressed by the following equation:

$$I = \alpha\omega^{\beta} \sum_{m} \sum_{n} \rho_{\gamma} [\langle \psi_m | \mathbf{d}_A | \psi_n \rangle \cdot \{\langle \psi_m | \mathbf{d}_B | \psi_n \rangle\}^*] \delta(\omega_{mn} - \omega) \tag{1.17}$$

where the sums run over all possible initial m and final n vibronic states, with ρ_{γ} being the Boltzmann population; δ is the Dirac function, and the asterisk is used to denote the conjugate of the $\mathbf{d}_{B,mn}$ matrix element. In the equation above, I is a general experimental observable related to intensity (e.g. for OPA, I is the molar absorption coefficient $\epsilon(\omega)$, and for OPE, I is the energy emitted by one mole per second I_{em}/N_n), and ω is the incident frequency. For OPA, OPE, ECD, or CPL, I is obtained by replacing α, β, γ, $\mathbf{d}_{A,mn}$, and $\mathbf{d}_{B,mn}$ according to

$$\mathrm{OPA}: \alpha = \frac{10\pi N_{\mathrm{A}}}{3\varepsilon_0 \ln(10)\hbar c}, \quad \beta = 1, \quad \gamma = m, \quad \mathbf{d}_{A,mn} = \mathbf{d}_{B,mn} = \mu_{mn}$$

$$\mathrm{OPE}: \alpha = \frac{2}{3\varepsilon_0 c^3}, \quad \beta = 4, \quad \gamma = n, \quad \mathbf{d}_{A,mn} = \mathbf{d}_{B,mn} = \mu_{mn}$$

$$\mathrm{ECD}: \alpha = \frac{40\pi N_{\mathrm{A}}}{3\varepsilon_0 \ln(10)\hbar c}, \quad \beta = 1, \quad \gamma = m, \quad \mathbf{d}_{A,mn} = \mu_{mn}, \quad \mathbf{d}_{B,mn} = \mathfrak{I}(\mathbf{m}_{mn})$$

$$\mathrm{CPL}: \alpha = \frac{8}{3\varepsilon_0 c^4}, \quad \beta = 4, \quad \gamma = n, \quad \mathbf{d}_{A,mn} = \boldsymbol{\mu}_{mn}, \quad \mathbf{d}_{B,mn} = \mathfrak{I}(\mathbf{m}_{mn})$$

In the formulas above, N_{A} is the Avogadro constant, ε_0 is the vacuum permittivity, μ_{mn} is the electric transition dipole moment between the vibronic states m and n, and $\mathfrak{I}(\mathbf{m}_{mn})$ is the imaginary part of the magnetic transition dipole moment between the vibronic states m and n. For a more detailed description of the theoretical background for calculating I for OPA, OPE, ECD, and CPL, the reader is referred to Refs. [47, 48].

In practical terms, in order to apply Eq. (1.17), additional approximations need to be introduced. Since analytical forms of transition moments are not known, they are usually expanded in power series with respect to the mass-weighted Cartesian normal coordinates $\mathbf{Q}$ about the equilibrium geometry of one of the electronic states:

$$\mathbf{d}_{X,mn}(\mathbf{Q}) = \mathbf{d}^{e}_{X,mn}(\mathbf{Q}_{\mathrm{eq}}) + \sum_{i=1}^{N} \left(\frac{\partial \mathbf{d}_{X,mn}}{\partial \mathbf{Q}_i} \right)_{\mathrm{eq}} + \cdots \tag{1.18}$$

where X can be either A or B. The expansion of Eq. (1.18) is usually truncated to the first two terms: the zeroth- and first-order first terms, which correspond to the FC approximation [50, 51] and Herzberg–Teller (HT) contribution [52], respectively. The VMS implementation includes both FC and HT terms, thus allowing the proper treatment of the leading contributions in both strongly and weakly allowed transitions.

Furthermore, the normal modes of initial and final electronic states are usually different and are related by the so-called Dushinsky transformation [53]:

$$\mathbf{Q} = \mathbf{J}\mathbf{Q}' + \mathbf{K} \tag{1.19}$$

where $\mathbf{Q}$ and $\mathbf{Q}'$ represent the mass-weighted normal coordinates of the initial and final electronic states, respectively, and $\mathbf{J}$ is the Dushinsky matrix, which describes the projection of the normal coordinate basis vectors of the initial state on those of the final state and represents the rotation of the normal modes upon the transition. Finally, the vector $\mathbf{K}$ represents the displacements of the normal modes between the initial and the final state structures.

Two general strategies are usually employed. These are the adiabatic model (adiabatic Hessian [AH]), which requires each PES being expanded around its corresponding energy minimum, and the vertical model (vertical Hessian [VH]), which needs the knowledge of both PESs expanded around the energy minimum of the reference electronic state. Further approximations can be obtained by neglecting mode-mixing and frequency change effects, thus leading the adiabatic shift (AS) and vertical gradient (VG) models, respectively. Furthermore, together with the time-independent (TI) sum-over-state approach, in the VMS software a time-dependent (TD) strategy, which employs the exact analytic form (at the harmonic level) of the time evolution, has been implemented [48]. The TI approach is the method of choice when high-resolution spectra are sought; however, it can suffer from convergence issues. These can be overcome with a TD approach, which takes into account all vibrational states, thus leading to fully converged spectra, possibly accounting for temperature effects, without any increase of the computational cost. Being based on the FC principle, the so far described framework is well suited to describe transitions accompanied by small structural changes, and it may fail when the flexibility of the system increases. A first improvement is obtained using internal coordinates instead of the Cartesian ones, because this choice minimizes the coupling between different modes even at an anharmonic level. A general implementation has been developed, which generates automatically a complete set of nonredundant internal coordinates starting from redundant generalized internal coordinates (GICs) [54]. Whenever a complete anharmonic treatment of the system is not feasible, an appealing approach is to divide normal modes in classes that are treated at different levels. This strategy can be efficiently applied, provided that large-amplitude motions (LAMs) can be decoupled from the remaining normal modes. In this respect, it has been shown that GICs provide an efficient reduction of mode couplings also for nontrivial LAMs [55].

1.2.2.4 Magnetic Spectroscopy

Spin relaxation techniques, such as NMR and ESR spectroscopies, represent powerful and sensitive tools for studying structural and dynamic properties of macromolecular systems. Among magnetic spectroscopies, we focus on ESR, often called electron paramagnetic resonance (EPR) spectroscopy, which is the spectroscopic technique of choice to investigate open-shell species. In particular, ESR is extensively applied to investigate complex biological systems, either directly or with the help of site-directed labeling techniques. In the following, we briefly summarize the theoretical aspects of ESR spectroscopy (a more detailed account can be found, for instance, in Refs. [56, 57]). When dynamical effects are not taken into account and only transition energies are considered, line positions

and the corresponding line intensities and amplitudes can be analyzed in terms of an effective spin Hamiltonian [58, 59]. The interaction of the electron spin (S) of a radical containing a nucleus of spin I with an external magnetic field ($\mathbf{B}$) can be approximated by the spin Hamiltonian H_s:

$$H_s = \mu_B S \cdot \mathbf{g} \cdot \mathbf{B} + S \cdot \mathbf{A} \cdot I + \cdots \tag{1.20}$$

where the first term is the Zeeman interaction between the electron spin and the external magnetic field in terms of the Bohr magneton, μ_B, and the electronic $\mathbf{g}$-tensor. Additional terms that might appear in the equation above are the spin coupling ($\mathbf{J}$) and spin–spin dipolar tensor ($\mathbf{T}$), which are present only when the system under consideration contains more than one unpaired electron (e.g. in the case of biradicals). The second term of Eq. (1.20) is the hyperfine interaction between S and I, described through the hyperfine coupling tensor $\mathbf{A}$, which in turn can be decomposed into two terms:

$$\mathbf{A} = a_K \mathbf{1} + \mathbf{A}_{\text{dip}}^{(K)} \tag{1.21}$$

where the first contribution is the isotropic hyperfine coupling constant (hfcc), while the second term is the anisotropic hyperfine coupling tensor. The former is the so-called Fermi contact term, which is related to the spin density at the Kth nucleus under consideration [60]

$$a_K = \frac{8\pi}{3} \frac{g_e}{g_0} g_K \beta_K \sum_{\mu\nu} P_{\mu\nu}^{\alpha-\beta} \langle \phi_\mu | \delta(\mathbf{r}_{nK}) | \phi_\nu \rangle \tag{1.22}$$

while the anisotropic contribution, also denoted as dipolar hyperfine coupling term, can be derived from the classical expression of interacting dipoles [61]:

$$A_{ij}^{(K)} = \frac{g_e}{g_0} g_K \beta_K \sum_{\mu\nu} P_{\mu\nu}^{\alpha-\beta} \langle \phi_\mu | r_{nK}^{-5} (r_{nK}^2 \delta_{ij} - 3 r_{nK,i} r_{nK,j}) | \phi_\nu \tag{1.23}$$

In both equations, $P_{\mu\nu}^{\alpha-\beta}$ is the difference between the density matrices for electrons with α and β spins, i.e. the spin density matrix, g_0 is the g-value of the electrons in the radical, and the ϕ's are the basis functions. Therefore, the essential quantities to be calculated are the spin density at the Kth nucleus and the dipole–dipole coupling terms. Consequently, isotropic and anisotropic hyperfine contributions can be easily evaluated as expectation values of the corresponding one-electron operators.

The electronic $\mathbf{g}$-tensor can be expressed in terms of second derivatives of the energy with respect to the external field ($\mathbf{B}$) and electron spin (S). The $\mathbf{g}$-tensor itself can be decomposed in its various contributions:

$$\mathbf{g} = g_e \mathbf{1} + \Delta\mathbf{g} \equiv g_e \mathbf{1} + \Delta\mathbf{g}_{\text{RMC}} + \Delta\mathbf{g}_{\text{DC}} + \Delta\mathbf{g}_{\text{OZ/SOC}} \tag{1.24}$$

where g_e is the free electron g factor (= 2.002319304386(20)), $\Delta\mathbf{g}_{\text{RMC}}$ is the relativistic mass correction, and $\Delta\mathbf{g}_{\text{DC}}$ is the gauge correction. These two terms are usually small and have opposite signs; as a consequence, their contributions tend to cancel out. The last term is a second-order contribution arising from the coupling of the orbital Zeeman (OZ) and the spin–orbit coupling (SOC) operators. Only the SOC term involves a true two-electron operator, but it is

usually approximated by a one-electron operator involving adjusted effective nuclear charges. An effective evaluation of the **g**-tensor for quite large systems by QC approaches is relatively recent and has been revolutionized by hybrid density functionals that, when coupled to proper basis sets, offer a very good compromise between accuracy and computational efficiency (see, for example, Refs. [62, 63]).

1.2.3 The VMS Framework: Quantum Chemical Methods

This section is focused on accuracy and interpretability. It is thus devoted to address the computational requirements for obtaining quantitative spectral prediction/analysis. The key point to reach this goal is to greatly reduce the errors associated with computations. This implies to reduce as much as possible the errors due to the truncation of both basis set and wavefunction, the so-called one- and N-electron errors, respectively. To fulfill this task, the best option is to rely on composite schemes, which are approaches that evaluate the contributions important to reach high accuracy at the best possible level and combine them through the additivity approximation [64–68].

For all spectroscopies, the starting point is an accurate and reliable description of the equilibrium structure, which is defined as a minimum on the Born–Oppenheimer (BO) PES. In this context, the best option is offered by the so-called semi-experimental (SE) equilibrium geometry (r_e^{SE}), which is obtained by a least squares fit of the experimental vibrational ground state rotational constants of different isotopic species corrected for computed vibrational corrections. In this respect, a new tool, the Molecular Structure Refinement (MSR) program [69], has been recently integrated in the VMS software. From a pure computational point of view, composite schemes based on coupled-cluster techniques including single and double excitations and a perturbative treatment of triples, CCSD(T) [70], and that account for extrapolation to the complete basis set (CBS) and core–valence (CV) correlation effects (i.e. the so-called CCSD(T)/CBS+CV scheme) are able to provide an accuracy similar to that offered by the SE approach [66, 67, 71]. To summarize, nowadays it is possible to determine equilibrium structures with an accuracy of 0.001–0.002 Å for bond lengths and 0.05–0.1° for angles. However, composite approaches are computationally expensive. It is therefore important to identify levels of theory that are affordable for medium- to large-sized systems. In this respect, the double-hybrid B2PLYP functional [72] in conjunction with triple-zeta basis sets is known to provide an accuracy of 0.002–0.003 Å for bond distances [73, 74], with maximum errors below 0.01 Å. Such an accuracy is well suited for subsequent spectroscopic applications.

Composite schemes can also be applied to the accurate computation of harmonic force fields. According to the literature on this topic (see, for example, Refs. [67, 75, 76]), composite approaches based on CCSD(T) are able to provide harmonic frequencies with an accuracy of 5–10 cm^{-1}. However, their applicability is limited to small- to medium-sized molecules. As in the case of equilibrium structures, B2PLYP in conjunction with triple-zeta quality basis sets provides an alternative for larger systems, thus showing an accuracy of 8–15 cm^{-1}. Due to the

computational requirements, the anharmonic part of force field calculations, i.e. the computation of cubic and quartic semi-diagonal force constants, is usually evaluated at a lower level of theory. While for small molecules the CCSD(T) method can be employed, when increasing the molecular size, global-hybrid (like B3LYP [77, 78]) or double-hybrid functionals are mostly used. Improvements in the accuracy can be achieved by means of hybrid approaches, where the harmonic part of the potential is determined at the CCSD(T) level or even employing a composite scheme, while for the anharmonic part Møller–Plesset theory to second order [79] and density functional theory (DFT) are used. When harmonic frequencies evaluated by means of composite schemes are combined with anharmonic corrections obtained using either B3LYP in conjunction with double-zeta quality basis sets or B2PLYP with triple-zeta quality sets, fundamentals as well as overtone and combination bands are predicted with mean absolute errors (MAEs) of 6–8 and 5–7 cm^{-1} (see, for example, Ref. [7]), respectively.

Analogously, hybrid approaches can also be applied to molecular and magnetic properties. In this case, CCSD(T) and composite schemes are used for highly accurate determinations of equilibrium values, with vibrational corrections computed using DFT approaches. A special note is required for magnetic properties. While it is well demonstrated that CCSD(T) is able to provide accurate results, the basis set issue is a delicate one in the view of obtaining quantitative predictions of the isotropic hfcc's. Indeed, to correctly describe the spin density at a nucleus, core correlation is necessary for atoms heavier than helium [80]. This is related to the general fact that very tight *s* primitives are needed to describe the spin density at the nucleus of interest as well as diffuse functions on surrounding atoms are required for a proper description of the spin density [80]. For these reasons, specific basis sets have been set up [81, 82].

Except for high-resolution gas-phase experiments, the recorded spectra are tuned by the surrounding environment (e.g. solvent, matrix, solid). A full QC treatment of a significant portion of the environment is in most cases not feasible, but more importantly, it is not even required. The experimental outcome corresponds to a statistical averaging of environment librations and small-amplitude motions, which, in turn, would require a huge number of barely feasible simulations. In addition, a full QC picture of the environment is not required to gain an accurate physical description of physical–chemical phenomena strongly localized in the probe. An effective strategy is then offered by focused models, where the system is partitioned into a chemically interesting core (e.g. the solute or a part of it) and the environment, which tunes the core's properties. A suitably high level of theory is retained for the core, whereas the environment is treated in a more approximate way. A popular focused approach is the so-called QM/MM model, where the core is treated by means of QC methods based on the coupled-cluster ansatz (or its equation of motion extension for excited states), whenever possible, or rooted in DFT (or TD-DFT for excited states) for larger systems; the environment retains its atomistic resolution, but it is described classically by a suitable molecular mechanics (MM) force field. In the last few years, a fully polarizable QM/MM/continuum approach, which employs a polarizable, fluctuating charge (FQ) FF, has been

developed to treat aqueous solutions [83–85]. This has been recently extended to linear response equations, first, second, and third analytical derivatives with respect to geometric and electric perturbations, which are the ingredients needed for a proper simulation of experimental spectra [86, 87].

1.3 The VMS Framework at Work

As mentioned in Section 1.1, VMS aims at going beyond the current approaches for the analysis and prediction of molecular spectra, i.e. VMS aims at moving from the standard practice of extracting numerical data from experiment to be compared with QC results to a direct comparison between the recorded and computed spectra. This strongly reduces any arbitrariness and allows for a proper account of all chemical–physical information hidden in the molecular spectra. The VMS software has therefore been devised to develop and implement efficiently spectral models able to account for all important vibrational and environmental effects in conjunction with the spectroscopic properties relevant to the technique under consideration as well as to include state-of-the-art QC computations of the latter. As mentioned above, in the following, we focus on rotational, vibrational, vibronic, and magnetic spectroscopies, thus providing an overview of the corresponding VMS modules.

1.3.1 Rotational Spectroscopy

Unlike other softwares purposely developed to support the analysis of MW spectra, the rotational spectroscopy module of the virtual multifrequency spectrometer, VMS-ROT, incorporates QC predictions to be used as starting points for guiding experiments and spectral interpretations. Indeed, in addition to provide a user-friendly access to the latest developments of computational spectroscopy, VMS-ROT is directly interconnected to the Gaussian package [14] as the reference source for the QC calculation of spectroscopic data. However, the extension to other QC packages, e.g. CFOUR [15], is in progress and will be available to external users in the next release. According to the user's expertise in performing QC calculations, the VMS-ROT allows for computations of any kind, ranging from standard geometry optimizations and frequency calculations to highly accurate composite schemes also including anharmonicity effects.

In the first step, i.e. the QC calculation of the relevant spectroscopic data, the user is supported by a "built-in tool" to automatically generate the required input files. In addition to this automatized procedure, the user can remove or add spectroscopic parameters as well as adjust manually their values. Once the results of the QC calculations are ready, the second step, i.e. prediction and/or fitting steps, relies on the SPFIT/SPCAT program developed by Pickett [88]. It should be noted that, while Pickett's program is the *de facto* standard for rotational and rovibrational analysis, sometimes the non-straightforward encoding of the spectroscopic parameters may prevent its immediate use. For this reason, VMS-ROT also provides an intuitive and user-friendly GUI for SPFIT and SPCAT, which

allows creating the required input files for the two programs, running them, and analyzing their output at the end of the execution. Once all the required data have been provided, the SPFIT/SPCAT program is executed, with the output details being displayed in a dedicated output textbox. At the end of this second step, the output files are automatically loaded in VMS-ROT. In the case of a fitting procedure, the new values of the spectroscopic parameters are displayed, whereas in the case of spectra prediction, the synthetic spectrum is shown in the plot area. If the first case applies, different tools are available for a fast and efficient analysis of the fitting process: (i) at each iteration, the trend of the root-mean-square (RMS) deviation of the fit is displayed in a dedicated plot; (ii) the correlation matrix among the spectroscopic parameters is graphically visualized as a gray-scale plot, where color saturation provides an intuitive indication of the absolute value, thus allowing one to quantify strong correlations between parameters that can lead to an ill-conditioned fit procedure; and (iii) a panel is devoted to the analysis of the residuals between observed and calculated transition frequencies, thus allowing the user to pick up, at runtime, those that deviate more than a specified threshold, thus permitting the quick identification of wrongly assigned lines. Once loaded in the plot area, the spectrum obtained in the third step (simulation or fit) can be edited by the user. To give an example, the stick spectrum can be convoluted with a suitable line shape function. The so-called VMS-Comparison tool can then be employed to compare computed and experimental spectra. This tool offers advanced manipulation utilities. It is worthwhile noting that if the experimental spectrum is the overall result of the concomitant presence of different species, e.g. conformers and isomers, then different computed spectra, one for each possibly present species, can be combined and weighted according to their relative population. Finally, VMS-ROT also incorporates all the required tools for the assignment of an experimental spectrum based on the predicted spectrum. A sketch of the so-called VMS-Assignment tool is graphically displayed in Figure 1.3, with the test case provided by the rotational spectrum of fenchone [89]. It is noted that the working area shows two horizontal panels: the calculated spectrum is depicted in the top one, whereas the experimental trace can be loaded in the lower panel. When both spectra are loaded into the corresponding panels, the assignment feature can be accessed by clicking on the proper item of the toolbar: for each assigned transition, the list of the upper- and lower-level quantum numbers, the measured and calculated frequency together with their difference, the estimated experimental uncertainty, and the weight of a transition within a blend of overlapped lines are annotated. Noted is that the assignment of a given experimental line, based on the comparison with the computed spectrum, can be performed in a manual or an automatic mode (this option is highlighted in Figure 1.3). Once a set of transitions has been assigned, it is then possible to proceed with the spectral fitting. A peculiar feature of VMS-ROT is that when the fitting process is completed, SPCAT is run as a background process with the newly determined parameters, thus allowing the update of the corresponding calculated spectrum. The spectral assignment procedure is iterated until a satisfactory assignment of the experimental spectrum is obtained.

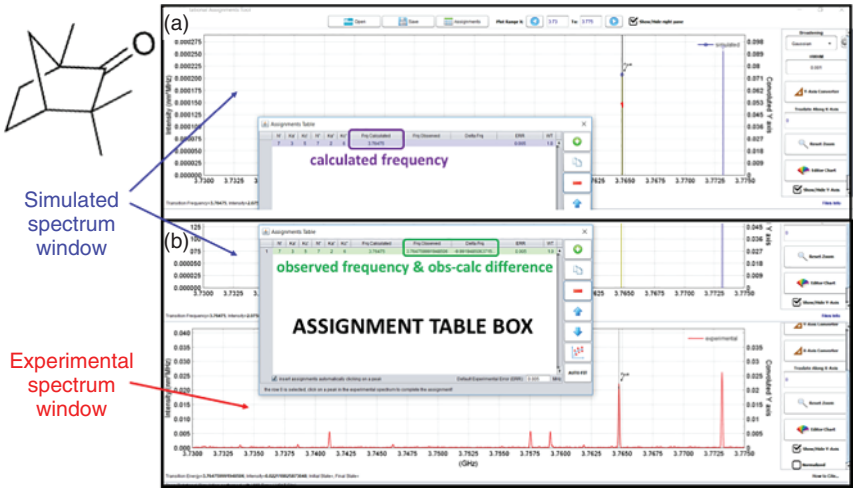

Figure 1.3 Assignment tool of VMS-ROT. (a) Simulated spectrum window: the selection of a transition in the calculated spectrum adds a new line in the assignment table, thus reporting the corresponding quantum numbers and calculated frequency of the selected peak. (b) Experimental spectrum window: the assignment is completed by selecting a transition of the experimental spectrum, which is added to the assignment table box.

As pointed out in the theoretical background, accurate equilibrium structures are the leading terms in the field of rotational spectroscopy. For this reason, the VMS-ROT module has also been equipped with the MSR code [69] for the accurate determination of molecular structures by means of the so-called SE approach [90]. While we refer the reader to the specific literature for a detailed description of the methodology (see, for example, Refs. [91, 92]), as already mentioned above, SE equilibrium geometries are obtained by a least squares fit of experimental vibrational ground state rotational constants of different isotopologues corrected by computed vibrational (and possibly electronic) contributions. The high accuracy of SE equilibrium structures (e.g. 0.001 Å for bond lengths) is well recognized in the literature [93]. However, this approach requires a sufficiently large number of isotopic substitutions in order to guarantee all structural parameters to be determined. When this condition may not be fulfilled, two strategies have been implemented in the MSR package. The first one is based on reducing the dimensionality of the problem by fixing a subset of the parameters to the corresponding QC values. In this respect, the availability of highly accurate geometrical parameters obtained from CCSD(T)-based composite models is a fundamental requisite. An alternative approach is provided by the so-called method of predicate observations [94], which implies to augment the input data set for the fit by estimates of structural parameters weighted appropriately.

1.3.2 Vibrational Spectroscopy

As described in the section dedicated to the theoretical background, the effects of mechanical, electrical, and, possibly, magnetic anharmonicity cannot be

neglected in order to obtain accurate vibrational frequencies and intensities, with VPT2 providing a cost-effective approach for fulfilling this task. As in the case of VMS-ROT, a vibrational spectroscopy module of VMS, VMS-VIB, is directly interconnected to the Gaussian package [14] as the reference source for both QC and VPT2 calculations. Since any meaningful comparison of computed spectra to experimental data requires the experimental conditions to be reproduced, the stick spectrum (a collection of peak positions and intensities) is convoluted with a line shape function (either Gaussian or Lorentzian) with a half width at half maximum (HWHM) suitably chosen. The convolution procedure is usually iterative, and it is performed by VMS-Draw, which is able to make adjustments in the HWHM, to plot the resulting computed spectrum and to compare it with the experimental one in real time. By performing the comparison between computed and experimental spectra, the selection of each peak in the stick spectrum directly provides its assignment to a specific transition. An example is shown in Figure 1.4, which compares experiment and theory for the IR spectrum of uracil recorded in Ar matrix in the 500–2000 cm^{-1} range [95], with the portion 1600–1800 cm^{-1} highlighted in the inset. It is first of all noted how well the experimental line shapes and their width are reproduced by the virtual spectrometer. Figure 1.4 also illustrates the inadequacy of the harmonic approximation to even qualitatively reproduce the experimental spectrum: not only the line positions are badly determined, but also – by definition – non-fundamental bands cannot be predicted. The level of theory employed is B3LYP-D3/SNSD, with D3 denoting Grimme's dispersion correction [96], which provides at the anharmonic level (i.e. VPT2 computations) a maximum absolute error of about 10 cm^{-1} for line positions.

In addition to spectra visualization, in VMS-VIB, other tools are available to analyze the outcome of anharmonic computations. The contribution of the higher derivatives to the anharmonic frequencies are collected in the so-called X matrix, which can be further split into different sub-matrices containing Coriolis, cubic, and quartic terms. Furthermore, the anharmonic correction for each mode can be split into intrinsic anharmonicity, direct coupling with each normal mode, and indirect coupling with more than one additional mode. The first two contributions are collected in the diagonal and off-diagonal elements of the Y matrix, respectively. All these matrices are visualized as gray-color scale plot, where the larger the matrix element is, the darker the color is. Such a visualization allows a quick quantification of all possible correlations between different groups of parameters, thus permitting to point out ill-conditioned optimizations. The analysis of anharmonic couplings provides important information on the system under study, and it can be used, for example, for defining cost-effective reduced dimensionality anharmonic models. To give an example, Figure 1.5 shows the heat diagram for the semi-diagonal cubic force constant K_{iij} matrix of glycine. Such diagram allows to describe the coupling between the normal modes, in particular the strong coupling between the symmetric NH_2 and the asymmetric CH_2 stretchings.

Molecular systems characterized by some flexibility show nearly isoenergetic isomers and/or conformers. Since these can be concomitantly present in experimental mixtures, the analysis of corresponding experimental spectra is

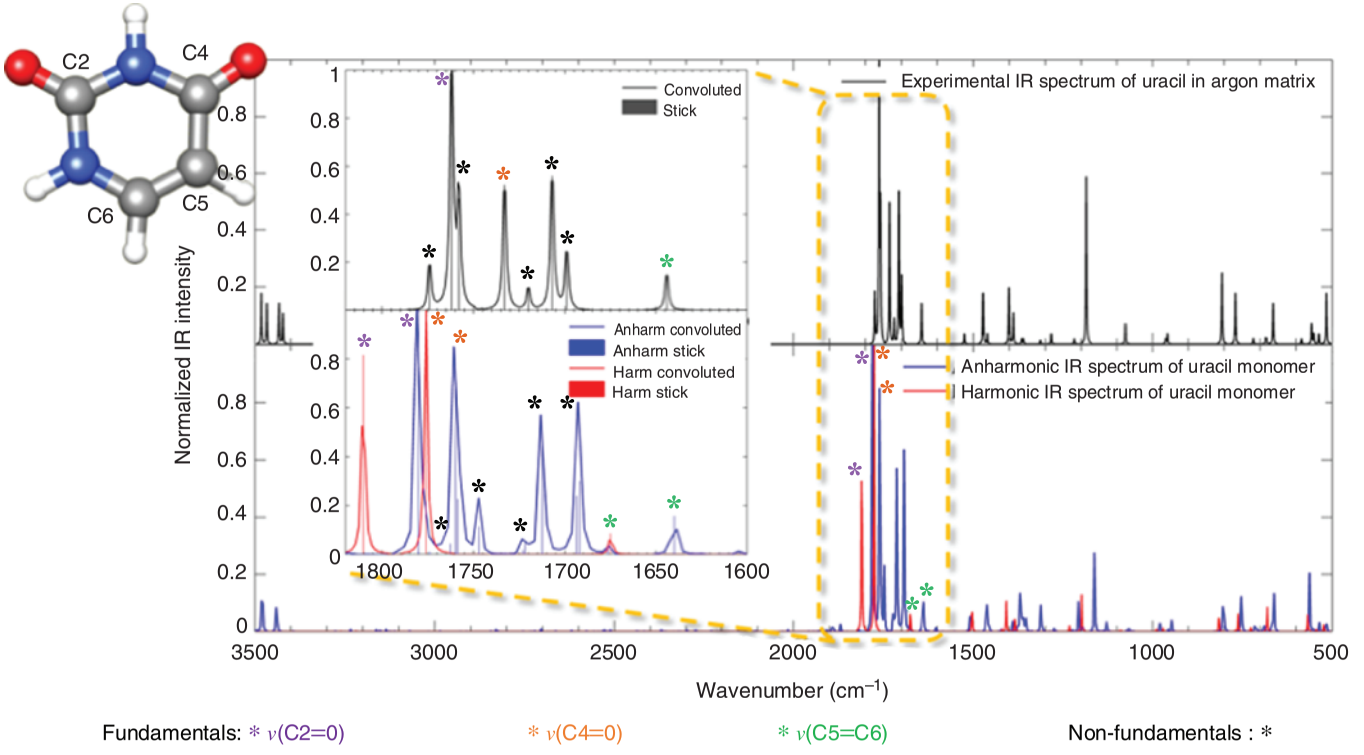

Figure 1.4 Comparison of the computed harmonic and anharmonic IR spectra of uracil to the experimental counterpart recorded in Ar matrix.

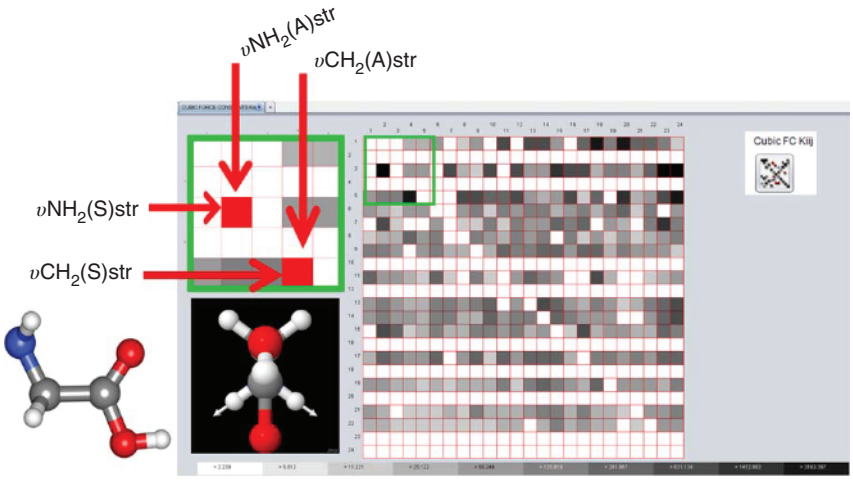

Figure 1.5 The heat diagram for the semi-diagonal cubic force constant, K_{ijj}, matrix of glycine.

further complicated by the fact that all of them should be taken into account based on their relative abundances. While we refer readers to the specialistic literature for the accurate computation of free energies (required for deriving the relative abundance) by means of composite schemes (see, for example, Refs. [67, 68, 97]) and for the approach to compute resonance-free thermodynamic properties beyond the RRHO model [37], we point out here the capability of VMS-VIB in dealing with vibrational spectra of complex molecular mixtures simulated based on the computation of the contributions for all conformers/isomers, weighted by theoretical Boltzmann populations. A specific example, the IR spectrum of glycine, will be discussed in Section 1.4.

VMS-VIB furthermore allows IR spectra to be converted from absorbance (which is proportional to the molar extinction coefficient, directly provided by most of the QC programs) to transmittance, which is the *de facto* standard for experimental recordings. However, since the conversion requires the knowledge of sample concentration and optical path, to avoid any inconsistency, the transmittance spectrum is provided in arbitrary units. In the case of Raman spectra, QC programs usually provide the Raman activity, whereas the principal experimental observable is the Raman cross section, with VMS-VIB allowing the plot of both quantities. In particular, the comparison of harmonic or anharmonic simulated spectra with their experimental counterparts can be performed by plotting the Raman cross section and adjusting the HWHM and line shape function of the peaks.

1.3.3 Vibronic Spectroscopy

As mentioned in the brief discussion of the theoretical background, a reliable description of molecular vibrations is of fundamental importance in both high- and low-resolution electronic spectra. In particular, the simulation of

vibrationally resolved electronic spectra is mandatory for correctly interpreting high-resolution experimental data in the gas phase that are characterized by intricate band shapes, which originate from the progressions of different vibrational motions. The situation is especially involved when investigating short-life molecules (e.g. free radicals), where different species can contribute to the overall recorded spectrum. In such circumstances the vibronic module of VMS can represent a valuable aid to experimentalists because the setup of the whole simulation is essentially completely automatized: starting from the QC computation of equilibrium geometries and harmonic force fields for all involved electronic states to the simulation of the whole spectrum and its comparison with its experimental counterpart, which can be imported in VMS by different means. Indeed, different tools for the analysis and visualization of results are implemented in VMS. An overall picture is provided by Figure 1.6: depending on the specific data set to be analyzed, different graphical representations, like two-dimensional (2D) or three-dimensional (3D) plots, bar charts, and heat maps, can be produced. More in detail, Figure 1.6 depicts the comparison between the vibrationally resolved computed (red) and experimental (blue) absorption electronic spectra of dideprotonated alizarin, with the scheme of the plot digitization procedure being also shown.

The present version of the software does not take into account all the effects tuning the spectral outcome (e.g. non-adiabatic couplings), but a pilot implementation of those contributions in the TD general framework has been recently completed [49] and will be available in the next release of VMS. Nevertheless, the current implementation has already allowed the simulation of qualitatively correct spectral line shapes, even when experimental data encompass large energy intervals and several excited electronic states. This is particularly true if vertical

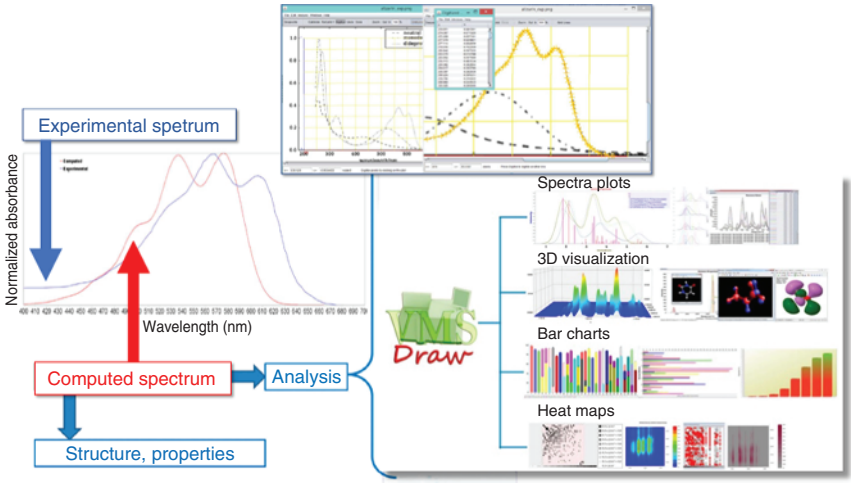

Figure 1.6 Comparison between the vibrationally resolved computed (red) and experimental (blue) absorption electronic spectra of dideprotonated alizarin, with the scheme of the plot digitization procedure being shown in the upper inset. In the right panel, a sketch of the different features available for analysis and visualization is depicted.

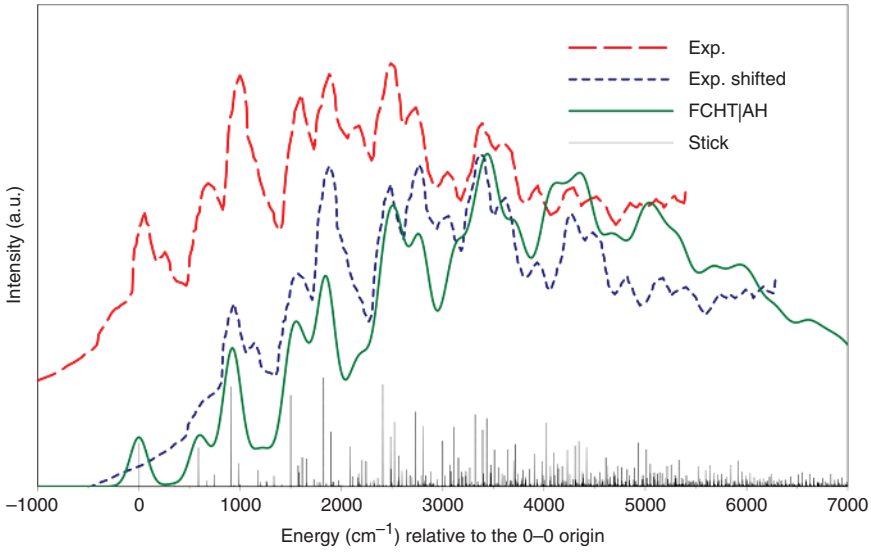

Figure 1.7 The A $^2B_1 \leftarrow$ X $^2A_1$ electronic transition of the phenyl radical in the gas phase.

excitations computed by refined post-Hartree–Fock approaches are evaluated at DFT/TD-DFT geometries, the latter approaches being employed also to obtain harmonic force fields. As an example, Figure 1.7 compares the simulated and experimental high-resolution spectra for the A $^2B_1 \leftarrow$ X $^2A_1$ electronic transition of the phenyl radical in the gas phase. It is apparent that the complete AH model including both Franck–Condon and Herzberg–Teller (FCHT) contributions provides results in remarkable agreement with experiment when the whole spectrum is slightly shifted in order to correct for some inadequacy of the computed vertical excitation energy (VE).

Vibronic effects play also a role in tuning the band shapes of less resolved electronic spectra, like those recorded in solution. In such circumstances, even when vibronic signatures are not apparent in the spectra, only inclusion of these effects allows for a correct evaluation of relative band intensities. Then, VMS provides an invaluable aid to experimentalists in setting up a proper computational strategy and in the comparison between computed and experimental spectra. To give an example, the UV–vis spectrum of the indigo dye (see Figure 1.8) is dominated by a single electronic transition, but the spectral shape is strongly nonsymmetric, and vibrational modulation plays a significant role both in this connection and in determining the color perceived by the human eye (see Figure 1.8).

Vibronic effects can be even more significant for chiral spectroscopies, in both absorption (ECD) and emission (CPL). An example is provided by the CPL spectrum of dimethyloxirane, which does not show any sign alternation at the FC level, but HT effects strongly modify the overall band shape and introduce a sign alternation (see Figure 1.9). In this case (and in a number of other circumstances), the robustness, flexibility, and ease of use of VMS allow for a detailed analysis of the different factors playing a role in determining the experimental outcome.

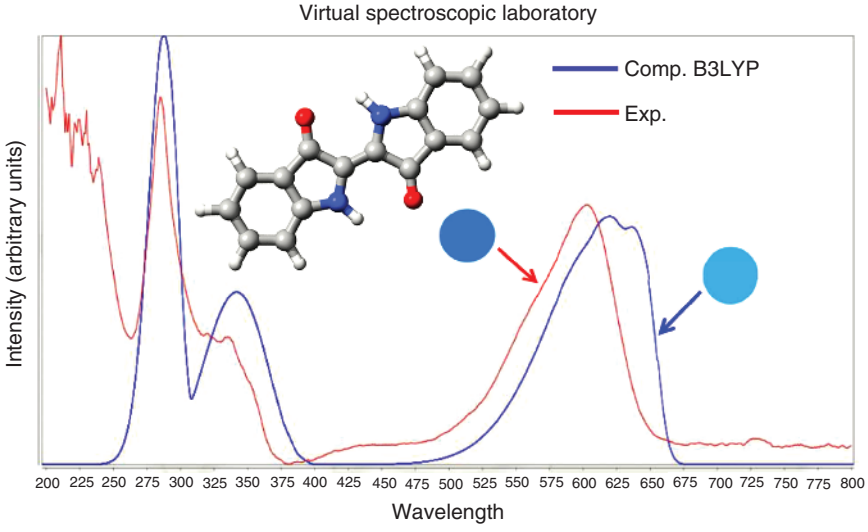

Figure 1.8 Comparison between the computed and experimental spectra of the indigo dye. Molecular structure is shown together with the color perceived by the human eye.

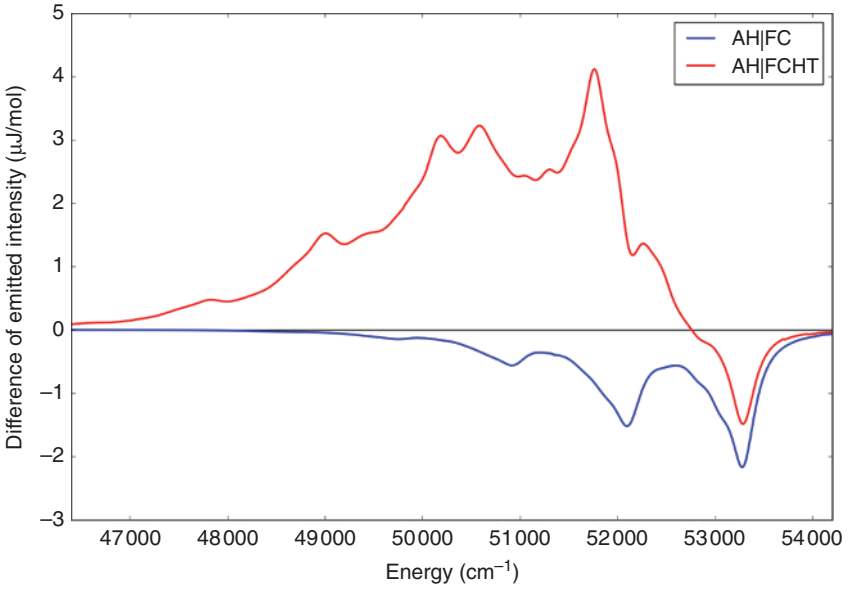

Figure 1.9 $S_3 \rightarrow S_0$ CPL spectrum of dimethyloxirane simulated by different models.

1.3.4 Magnetic Spectroscopy

As already mentioned, the VMS package contains two different tools for magnetic spectroscopy: one devoted to EPR and the other to NMR spectroscopy. In the context of magnetic spectroscopy, we focus on EPR, whose theoretical background has been briefly summarized in Section 1.2.2.4. The main features

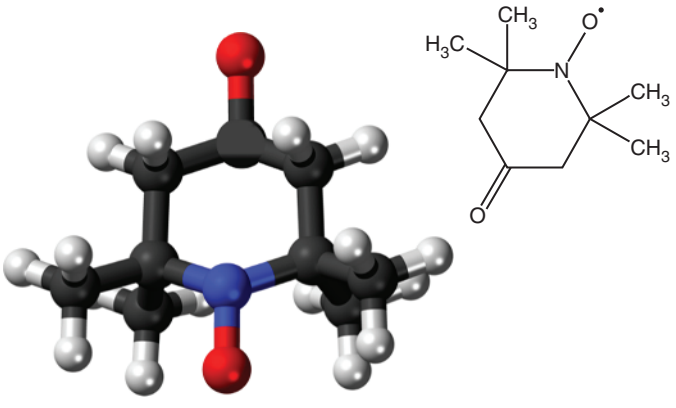

Figure 1.10 The 2,2,6,6-tetramethyl-4-piperidone-1-oxyl radical, also known as TEMPONE.

of VMS in the framework of EPR spectroscopy will be sketched with reference to the simulation of the EPR spectrum of the TEMPONE radical (see Figure 1.10), whereas we refer readers to Ref. [11] for a detailed account on the VMS-NMR tools.

As with all other spectroscopies, the starting point is the input of the target molecule set up by means of the general graphical utilities of VMS-Draw (which are shared by all the other modules) and the subsequent submission, in background, of the specific QC code, which is, for the purposes of this section, the Gaussian16 (G16) suite of programs for quantum chemistry [14]. Since TEMPONE is a molecule that at room temperature rapidly interconverts between two twisted-crossover structures, the electronic structure computations should include the averaging of the magnetic tensors over the effective LAM connecting these two geometries. The G16 software is able to perform automatically this task together with the perturbative treatment needed to take into account the vibrational averaging for all the other small-amplitude vibrations. The detailed procedure can be summarized by the following steps and a representative screenshot of the whole process is provided in Figure 1.11:

Step 1: A 3D graphical representation: The molecule is shown together with the inertial laboratory frame.

Step 2: By clicking on the "Set Dynamics" button, a new window is opened where the user can choose the form of the diffusive operator Γ, which describes the overall rotational motion of the probe (possibly coupled to large-amplitude internal rotations) at a coarse-grained level based on the model describing diffusive motions of regular bodies in viscous media [98]. In this case the one rigid body model can be chosen for the rotational averaging.

Step 3: By clicking on the "Spin Probes" button, a new window opens, thus allowing a user-friendly setting of the spin Hamiltonian parameters. The setting also includes the choice of the number of unpaired electrons and of the corresponding reference atoms (in the present case, the selection is one electron and the N–O moiety, which defines the reference frame

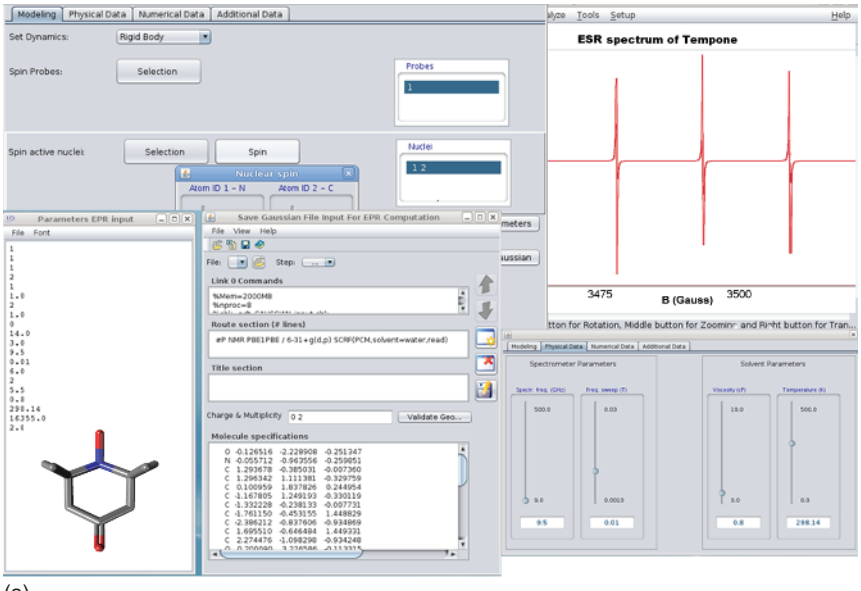

(a)

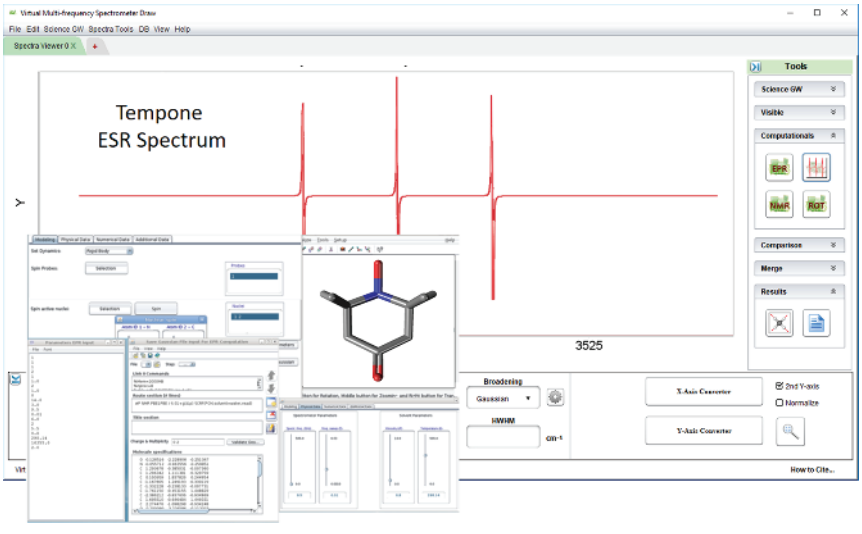

(b)

Figure 1.11 Two representative screenshots of the VMS-EPR software: setup of the modeling parameters (a) and of the spectra viewer (b).

for the **g**-tensor), and it also permits the indication whether spin active nuclei are possibly present in the probe(s) (in the present case, the N atom with nuclear spin 1), which leads to the drawing of the reference frame for the **A**-tensor.

Step 4: In the "Physical Data" tag of the "Parameter Selector," a number of relevant parameter are set, also including the magnetic field (**B** = 3197.3

G in the present case), the field sweep (75.7 G), the viscosity of the solvent (water in the present case: $\eta = 0.89$ cP), and the temperature ($T = 298.15$ K).

Step 5: The "Additional Data" tag is used to set the intrinsic linewidth to 2.4 G, which is a typical value since the unresolved super-hyperfine coupling of the electron with 12 surrounding hydrogen atoms has to be taken into account.

Step 6: Clicking on the "Diffusion" button in the "Main Control" panel activates the automatic computation of the diffusion tensor and the appearance of the corresponding reference frame in the 3D space, with atoms assuming different colors if they belong to different fragments. In the present case (i.e. a single fragment), all atoms have the same color.

Step 7: In the "Diffusive Environment," the magnetic tensors can be provided or modified from the values already available to the program by previous quantum mechanical computations. Next, their values can be adjusted by fitting within the "Refine Environment." It should be noted that in general small corrections, at most, are necessary and, in the present case, the traces of g and $\mathbf{A}$ have been slightly adjusted together with the intrinsic linewidth.

Step 8: By clicking the "Load Spectrum" button, an experimental spectrum is loaded, and it can be manipulated by using the general VMS utilities.

Step 9: Now the user is ready to enter the "ESR Environment," where spectra can be calculated (by setting up and solving the stochastic Liouville equation (SLE) [98]) with or without fitting the experimental counterpart and then plotted. Note that it is possible to run the calculation interactively or via Portable Batch System (PBS). In the present case, very small corrections (<0.1%) to the refined parameters have been obtained.

Step 10: The theoretical and experimental spectra are visualized and can be shifted, scaled, etc. by using the general VMS tools.

1.4 The VMS Framework: Applications

To address the great potentialities of the VMS software, four case studies have been selected. The choice has been made in order not only to point out the ability of VMS in dealing with different spectroscopic techniques and thus providing an exhaustive characterization but also to demonstrate the scientific impact of VMS in the field. The first two case studies concern glycine and methyloxirane. For both of them the spectroscopic characterization starts from an accurate structural determination and involves rotational and vibrational spectroscopies. In the third case study, the spectroscopic investigation is extended to electronic spectroscopy, pyrimidine being the molecular system chosen. The fourth case study deals with the EPR spectra of Fmoc-(Aib-Aib-TOAC)$_2$-Aib-OMe in different solvents, thus showing how structural information can be derived from accurate spectral simulations.

1.4.1 A Complete Spectroscopic Characterization: The Glycine Case Study

Glycine (H_2NCH_2COOH) is the simplest amino acid, and it is probably the most natural prototypical system for analyzing the intrinsic structural and conformational characteristics of a peptide and protein backbone without the perturbing effect of lateral chains. For this reason, it has been the subject of an increasing number of experimental and theoretical investigations (see Ref. [67] and references therein). Although the zwitterionic structure is the most stable form of glycine in condensed phases, the neutral form is significantly more stable in the gas phase. To fully spectroscopically characterize a molecular system, the first important step is an accurate determination of its equilibrium structure. As already mentioned, composite schemes on the pure computational side and the SE approach from an experimental point of view are able to provide very accurate equilibrium geometries. Based on Refs. [67, 69, 99], it can be pointed out that even when there is a lack of experimental information, the so-called method of predicate observations allows for accurately characterizing the molecular structure of medium-sized molecules. This method has been effectively implemented in the MSR software, which in turn is integrated in VMS. Figure 1.12 shows a snapshot of the user-friendly graphical interface of MSR and the rich information provided.

As addressed in the theoretical section, an accurate equilibrium structure determination is at the heart of the characterization by means of rotational spectroscopy, which can be carried out by the VMS-ROT module, as described in Section 1.3.1. The accuracy that can be obtained has been demonstrated in Ref. [100]: from the comparison to experimental data for the Ip/ttt conformer (i.e. the most stable one), it is noted that when a composite scheme is employed, the rotational constants are reproduced with discrepancies of about 0.1–0.2%.

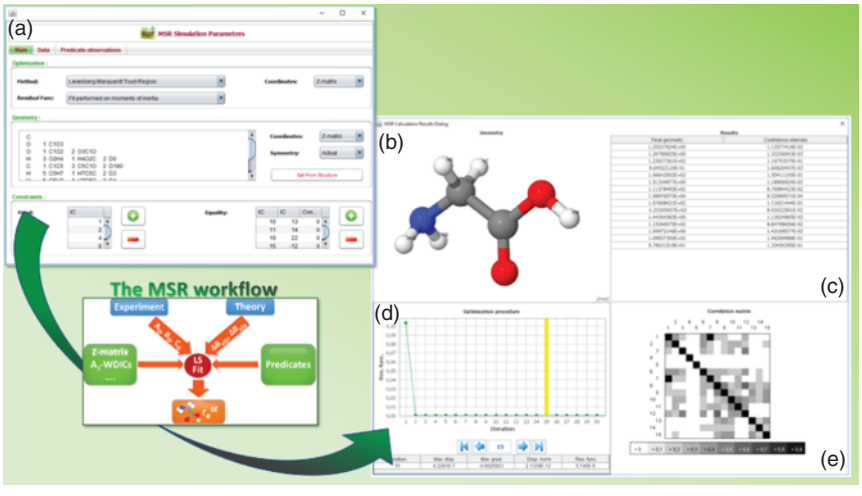

Figure 1.12 The MSR software: (a) input panel, (b), visualization panel, (c) results panel, (d) optimization trend panel, and (e) correlation matrix panel.

The same accuracy is expected for the [OD,ND_2] trideuterated isotopologue, for which experimental data are missing and could be instead straightforwardly derived by means of VMS-ROT. In Ref. [100], other rotational spectroscopy parameters, like centrifugal distortion and nuclear quadrupole coupling constants, were investigated. Also for them, VMS-ROT is able to determine values that fulfill the so-called spectroscopic accuracy.

Glycine is a rather flexible molecule; as a consequence, a gas-phase sample is characterized by the concomitant presence of different conformers, whose abundance is related to the relative stability. Therefore, an important issue is the accurate determination of the thermochemical properties of the mixture under investigation. While we refer the reader to Ref. [67] for a detailed account on the energetics of glycine, we discuss here the impact that the presence of different conformers has on its IR spectrum. The IR spectrum for a mixture of conformers can be accurately simulated by using VMS-VIB. An example, for glycine at the temperature of 410 K, is provided by Figure 1.13, which compares the simulation for a mixture containing the Ip/ttt, IIn/ccc, IIIp/tct, IVn/gtt, Vn/gct, and VIp/ttc to the corresponding experimental counterpart for both the main isotopologue and the [OD,ND_2] trideuterated isotopic species. The figure also shows the simulation of the IR spectrum when accounting for only the three most stable conformers, namely, Ip/ttt, IIn/ccc, and IIIp/tct. It is observed that the experimental spectrum is well reproduced by the latter simulation, but a closer inspection (see the inset of Figure 1.13) demonstrates that small but non-negligible features appear when also the other three conformers are considered. For a detailed account, interested readers are referred to Ref. [67].

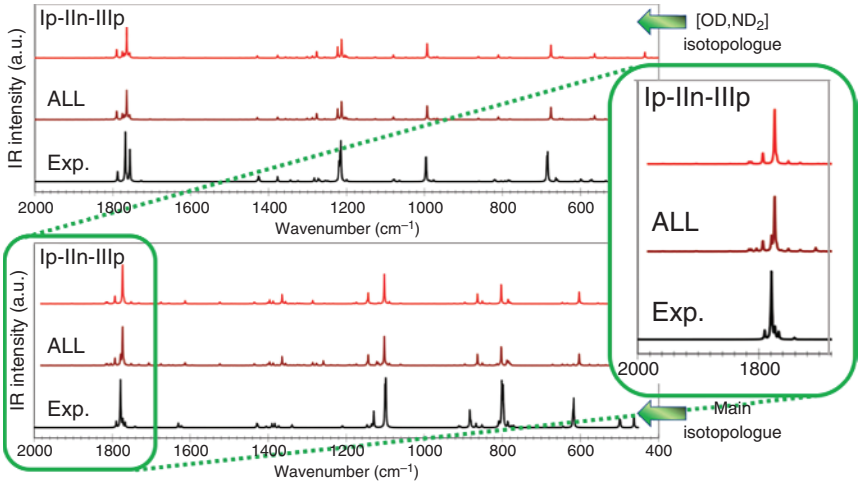

Figure 1.13 Simulated theoretical spectra: "ALL" (dark red) means the sum of the Ip/ttt, IIn/ccc, IIIp/tct, IVn/gtt, Vn/gct, and VIp/ttc spectra, and "Ip-IIn-IIIp" (red) means the sum of the Ip/ttt, IIn/ccc, and IIIp/tct contributions, both weighted for relative abundances. In black the experimental spectrum. Lower panel: main isotopologue; upper panel: trideuterated isotopic species. In all cases, $T = 410$ K. Source: Ref. [101].

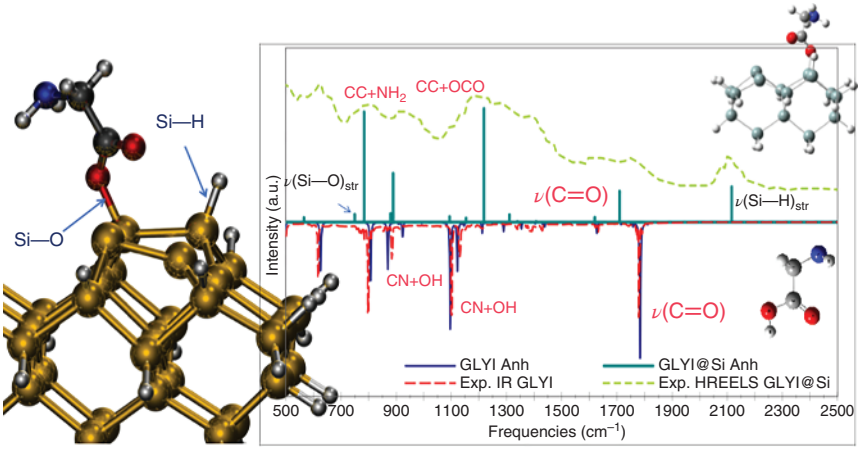

Figure 1.14 Comparison of gas-phase and chemisorbed glycine spectrum to experiment.

Another aspect of interest, for instance, to astrochemistry, concerns the interaction of biomolecule building blocks with different substrates mimicking meteorites or ices. In such cases, the flexibility of VMS can be employed to treat the probe molecule (and, if needed, its local environment on the substrate) at the anharmonic level, while the substrate (or its remaining part, if a local portion is better treated) is described at the harmonic level. This is the so-called reduced dimensionality approach, and it allows for investigating quite large systems, also taking into account the most important couplings between the probe and the substrate. As an example, Figure 1.14 compares the simulated IR spectrum of glycine in the gas phase and that obtained when it is chemisorbed on the (100) surface of silicon (modeled by means of a Si_{15} cluster) to their experimental counterparts [102]. It is noted that the remarkable agreement with experiment allows an unbiased analysis of the spectral shifts in terms of well-defined physical–chemical effects.

1.4.2 Vibrational Spectroscopy of a Chiral Molecule: The Methyloxirane Case Study

Substituted oxiranes are the *de facto* standards for benchmark theoretical and experimental methodologies for chiroptical spectroscopies. Among them, methyloxirane plays a central role, and for this reason it has been extensively investigated (see Ref. [103] and references therein). Accurate molecular structures and vibrational spectra are the mandatory starting points for an accurate treatment of chiroptical spectroscopies. Indeed, the positions of the VCD bands are the same as those of their IR counterparts, and the VCD intensities depend, in addition to the magnetic moments, on the electric moments involved in the IR intensities. At the same time, optical activity is ruled by molecular structure and vibrational effects. Furthermore, chiral and non-chiral molecular properties as well as thermodynamical functions are in all cases obtained from the same anharmonic force field employed in the IR spectra determination.

As already pointed out, for an accurate comparison with experimental data, it is necessary to go beyond the double harmonic approximation, thus allowing for the consideration of overtones and combination bands. Indeed, to give an example, the simulation of fully anharmonic spectra gives the possibility to correctly assign low-intensity fundamentals and distinguish them from non-fundamental transitions that might lie nearby. For chiral molecules, this strategy is particularly effective if "standard" vibrational spectroscopies, e.g. IR and Raman, are combined with VCD and vibrational Raman optical activity (VROA).

To simulate IR spectra, in particular, when aiming at a direct vis-à-vis comparison with experiment, reliable relative intensities along with accurate band positions are mandatory to obtain a correct spectral line shape/intensity pattern. The investigation of methyloxirane and other substituted oxiranes reported in Ref. [103] provides a perfect test case to focus on the convergence of simulated IR spectra at different level of theory. For methyloxirane, this is well presented in Figure 1.15, where the simulated IR spectra obtained by means of different hybrid force fields are shown. Hybrid force fields are usually derived in a normal coordinate representation by replacing in the full anharmonic force fields computed at a low level of theory (usually at the DFT level) the harmonic wavenumbers calculated at a higher level of theory (for example, by means of a composite scheme based on coupled-cluster theory, denoted as CC in the present case). First of all, it is noted that spectra simulated with vibrational wavenumbers computed at the CC/B2PLYP level are very similar, irrespective of the correction for IR intensities at the harmonic level with best estimates (CC/B2PLYP Freq+Int) or not (CC/B2PLYP). The good accuracy of all hybrid force fields, and in particular

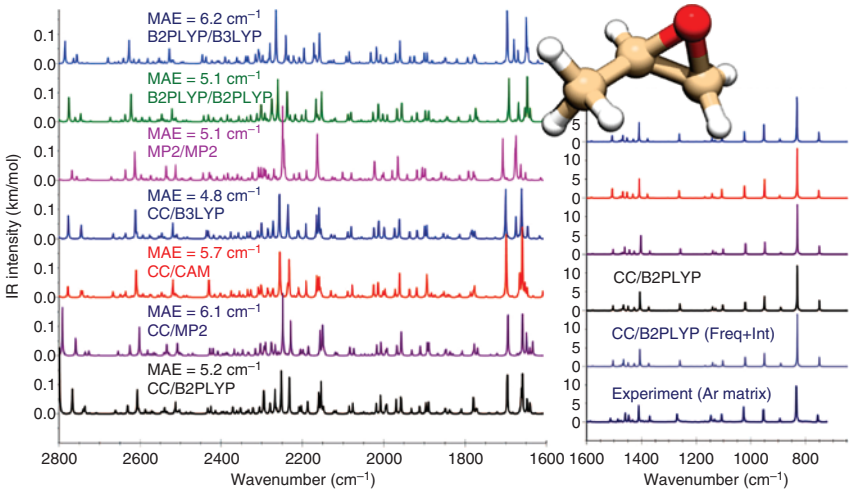

Figure 1.15 Anharmonic IR spectra of methyloxirane in the 1600–2800 and 700–1600 cm^{-1} ranges computed using different hybrid schemes, together with the corresponding maximum absolute error (MAE) with respect to experiment. For the latter range, the comparison with experiment is also reported. Simulated spectra line shapes are convoluted with Lorentzian distribution functions with a HWHM of 1 cm^{-1}.

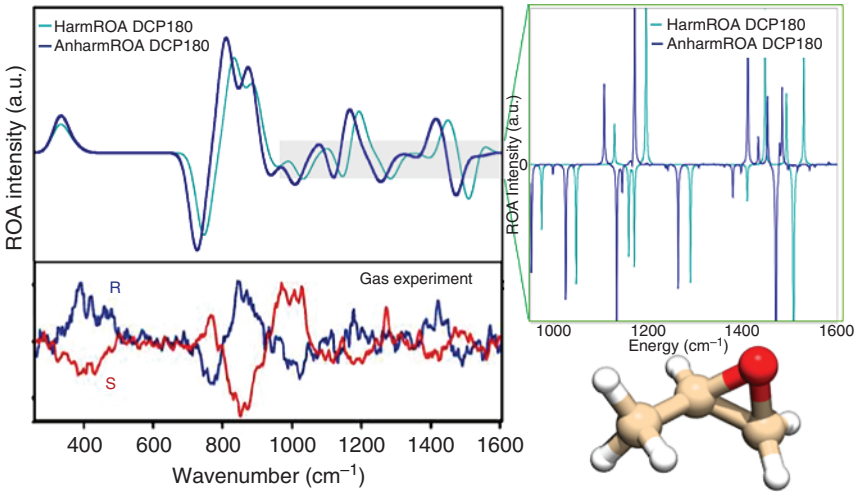

Figure 1.16 Fully anharmonic ROA spectrum of (R)-methyloxirane compared with its experimental counterpart measured in gas phase. Vibrational wavenumbers have been computed at the CC/B3LYP level [103] in conjunction with B3LYP intensities. Simulated spectra have been convoluted by means of Lorentzian distribution functions with full width at half maximum (FWHM) of 2 cm^{-1}.

of that denoted CC/B2PLYP, is confirmed by the comparison with experiment [104]. Indeed, all hybrid models with the harmonic part computed at least at the B2PLYP level reproduce well the results obtained with the best estimated harmonic force field, with the B2PLYP/B3LYP model providing fairly good estimates of IR spectra up to 6000 cm^{-1}.

Thanks to recent developments of VMS [13], it has been possible to simulate the ROA spectrum of methyloxirane in the gas phase including both mechanical and electric/magnetic anharmonicities in the framework of GVPT2, also taking into full account all first- and second-order resonances. The comparison with the corresponding experimental spectrum [105], depicted in Figure 1.16, shows a remarkable agreement in terms of both band positions and overall spectral shape [13]. On the contrary, the corresponding simulation at the harmonic level leads to quite disappointing results because several bands are missing and the positions of the others are often significantly blueshifted. The availability of reliable simulations of ROA spectra in the gas phase is important in view of the considerable difficulties usually encountered in their experimental recording. Indeed, such an accuracy opens to the effective interpretation of experimental spectra in aqueous solution, which can be simulated by adding a discrete–continuum description of the solvent, in terms of intrinsic and environmental effects.

1.4.3 From Molecular Structure to Electronic Spectrum: The Pyrimidine Case Study

As a further case study, we present a complete characterization of pyrimidine, a semirigid molecule, which represents the backbone of some DNA bases and for which a number of high-resolution spectra in the gas phase are available.

In Ref. [106], an integrated computational approach combining QC methods, purposely tailored inter- and intramolecular force fields, and continuum solvent models combined with TI and TD schemes to account for nuclear motion effects was applied to the spectroscopic study of pyrimidine in the gas phase as well as in aqueous and CCl_4 solutions. In addition to its scientific significance, that investigation is also illustrative of the great advantages provided by VMS. Indeed, that study was extremely time consuming, it required a large effort, and it involved a large number of scientists. Nowadays, the availability of the VMS software would greatly reduce all possible efforts, thus opening complete spectroscopic characterization of even more involved systems.

As mentioned above, the starting point of a spectroscopic study is the accurate evaluation of the molecular structure. For pyrimidine, a selection of computational and SE determinations is given in Table 1.1, along with a graphical representation and the corresponding atom labeling scheme. In Ref. [106], to accurately compute the equilibrium structure of pyrimidine, the CCSD(T)/CBS and CCSD(T)/CBS+CV composite approaches were employed. The rotational spectra of different isotopic species of pyrimidine were investigated [107]. This allowed for the derivation of an SE equilibrium structure. However, the lack of experimental data for deuterated species did not permit the determination of a complete SE geometry, indeed not allowing the C—H bond lengths to be determined. In the meantime, two models have been proposed to effectively deal with these situations. In the first one, the so-called template molecule (TM) approach [92], some parameters are fixed at the values optimized at a reasonable QC level (B3LYP/SNSD in the present case) and corrected for the inaccuracy of the model using the information for a similar molecule (here pyridine), whose full SE structure is available. In the present context, in addition to the three C—H bond lengths, also the $\angle H_2–C_2–N$ valence angle had to be fixed. The second approach, which is referred to as linear regression (LR) model [73], exploits the systematic nature of the errors on bond lengths computed by hybrid or double-hybrid density functionals (B3LYP/SNSD and B2PLYP/cc-pVTZ in the present case) to build LR using the large number of molecules whose full SE structures are available. Since LRs for individual valence angles are less reliable, improved accuracy and robustness were obtained by employing the difference (δ) between the two valence angles formed by a substituent to an sp^2 carbon atom. In this case, in addition to the three C—H bond lengths, the δ_4 angle difference was kept fixed. From Table 1.1, it is noted that the agreement between the SE structures obtained by means of both the TM and LR models and the CCSD(T)/CBS+CV equilibrium structure is remarkable, thus confirming the accuracy and reliability of the approaches employed.

Moving to the study of the IR spectrum of pyrimidine, we first of all note that the dimension of the molecule permits the use of the most refined hybrid procedures we have at our disposal, in which harmonic frequencies (and intensities) computed at the CCSD(T) level are supplemented by anharmonic contributions evaluated at the B3LYP/SNSD or, better, B2PLYP/maug-cc-pVTZ levels. The whole set of force constants (up to semi-diagonal quartic) and dipole derivatives (up to semi-diagonal cubic) are used to compute the IR spectrum by using the GVPT2 approach [33, 40]. The results obtained for pyrimidine [106] are in line

Table 1.1 Equilibrium structure of pyrimidine (bond lengths in Å, angles in degrees).

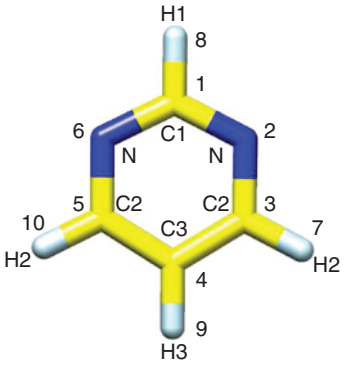

Parameter	*Ab initio* Ref. [106]		Semi-experimental Ref. [73]		
	CCSD(T)/ CBS	CCSD(T)/ CBS+CV	B3LYP/[a] SNSD [TM]	B3LYP/[b] SNSD [LR]	B2PLYP/[b] cc-pVTZ [LR]
C_1–N	1.3351	1.3329	1.3334(1)	1.3334(3)	1.3333(3)
N–C_2	1.3363	1.3341	1.3355(1)	1.3353(2)	1.3350(2)
C_2–C_3	1.3891	1.3868	1.3867(3)	1.3869(3)	1.3868(2)
C_1–H_1	1.0831	1.0820	1.0822[c]	1.0820[c]	1.0820[c]
C_2–H_2	1.0837	1.0826	1.0826[c]	1.0825[c]	1.0825[c]
C_3–H_3	1.0806	1.0795	1.0795[c]	1.0794[c]	1.0794[c]
$\angle C_1$–N–C_2	115.69	115.75	115.69(1)	115.69(1)	115.70(1)
$\angle$N–C_2–C_3	122.31	122.28	122.27(2)	122.27(1)	122.27(1)
$\angle C_2$–C_3–C_2	116.64	116.65	116.72(1)	116.71(1)	116.70(1)
$\angle H_1$–C_1–N	116.32	116.36	116.31(1)	116.31(1)	116.32(1)
$\angle H_2$–C_2–N	116.43	116.46	116.37[c]	116.53(1)	116.52(1)
$\angle H_3$–C_3–C_2	121.68	121.67	121.64(1)	121.65(1)	121.65(1)
δ_4			2.49	2.34[c]	2.34[c]

a) For the non-determinable parameters, the TM approach was used. See text.
b) For the non-determinable parameters, the LR approach was used. See text.
c) Values kept fixed.

with those computed for several other molecules of similar dimensions (see Figure 1.17) and allow an unbiased analysis of the experimental data including fundamentals as well as overtones and combination bands. In the specific case of pyrimidine, since there are not strong resonances, the analysis in terms of normal modes turned out to be quite straightforward.

The next spectroscopy to be considered is UV–vis. The starting point is the analysis of VEs in order to investigate the reliability of different electronic structure models. Using the geometries discussed above, the VEs have been computed for a number of singlet states using both TD-DFT (Cam-B3LYP functional)

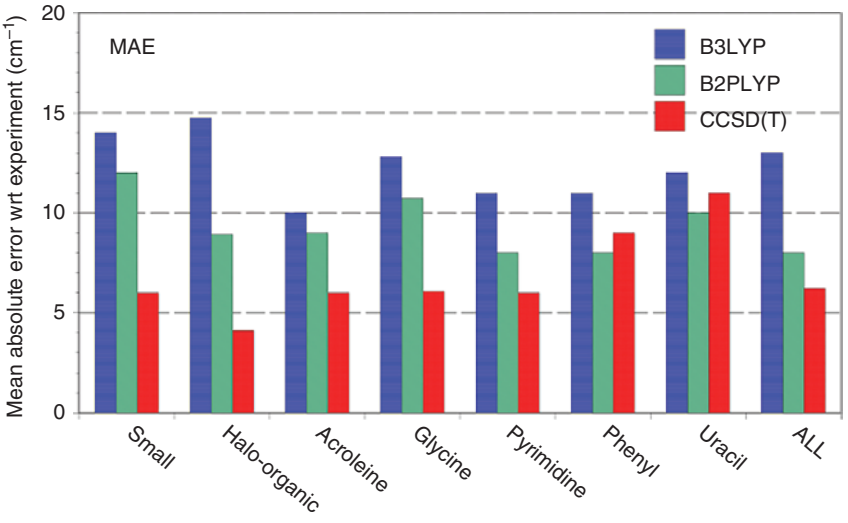

Figure 1.17 Performance of the B3LYP/SNSD, hybrid B2PLYP/B3LYP, and CCSD(T)/B3LYP models for the computation of anharmonic vibrational wavenumbers by means of the GVPT2 approach. All anharmonic corrections have been computed at the B3LYP/SNSD. Harmonic wavenumbers at the B2PLYP and CCSD(T) levels have been computed with basis sets of at least triple-zeta quality.

and the multi-reference variational/perturbative (MRPT) approaches, which are implemented in the BALOO code [109]. The comparison with the available experimental data (see Table 1.2) demonstrates that MRPT computations are extremely reliable for the low-lying excited singlets and that can be used to correct TD-DFT VEs prior to their use in vibronic computations.

Let us now take into account vibrational modulation effects in the portion of the absorption spectrum corresponding to the $S_1 \leftarrow S_0$ transition by means of the models described in the theoretical background section. Since a gas-phase high-resolution spectrum is available [108], the most refined approach at our disposal was employed, thus combining the MRPT VE with the vibrational frequencies of the electronic ground state issued by the hybrid scheme described above and the TD-DFT harmonic frequencies of the S_1 state corrected by means of an effective scaling procedure described, for instance, in Ref. [110]. It is worthwhile noting that the energy minimum of the S_1 state is not planar; as a consequence, a more rigorous approach should take into proper account the large-amplitude ring-inversion motion, with the latter being treated by a proper model. While work is in progress in this direction, a simplified procedure based on an effective harmonic oscillator treatment was employed, which gives reasonable results in the case of low inversion barriers (in the present case, around 70 cm^{-1}). The comparison between experimental and simulated spectra is given in Figure 1.18, and a remarkable agreement is indeed noted. According to computations, the most intense absorptions correspond to the in-plane ring deformations of A_1 symmetry (ν_7, ν_8, and ν_9 modes of the ground electronic state), and the main

Table 1.2 Vertical excitation energies and oscillator strengths for the low-lying excited singlets of pyrimidine.

Assignment	Symmetry	TD-DFT[a] VE (eV)	TD-DFT[a] Oscillator strength	MRPT[b] VE (eV)	MRPT[b] Oscillator strength	Experiment[c] VE
$\pi^* \leftarrow n_N$	B_1	4.58	0.0062	4.19	0.0042	4.18
$n_N \leftarrow n_N$	A_2	4.94	0.0000	4.59	0.0000	4-5
$\pi^* \leftarrow \pi^*$	B_2	5.85	0.0453	5.16	0.0380	5.22
$\pi^* \leftarrow n_N$	A_2	6.03	0.0000	5.68	0.0000	
$\pi^* \leftarrow \pi^*$	B_1	6.33	0.0059	5.99	0.0034	~6
$\pi^* \leftarrow \pi^*$	A_1	6.71	0.0402	7.02	0.0715	6.69
$\pi^* \leftarrow \pi^*$	A_1	7.63	0.2292	7.79	0.4504	7.48
$\pi^* \leftarrow \pi^*$	B_2	7.84	0.4003	8.13	0.5118	

a) Cam-B3LYP/aug-N07D.
b) 6-31G(d) basis set.
c) Ref. [108].

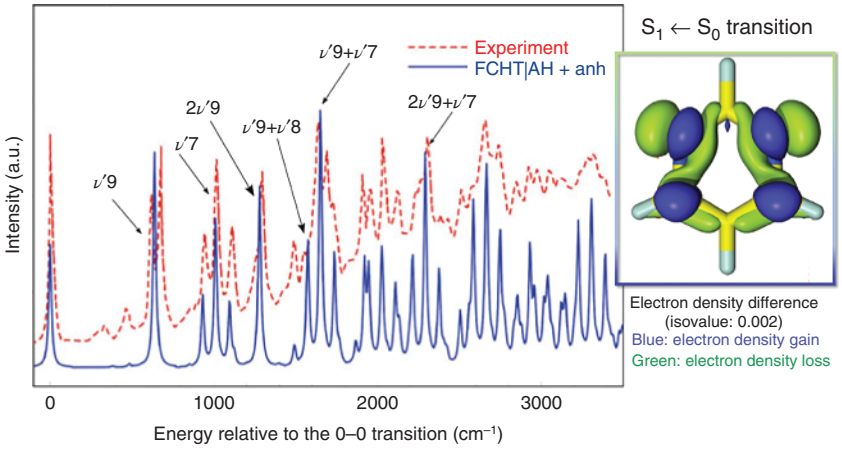

Figure 1.18 Computed and experimental spectra for the $S_1 \leftarrow S_0$ transition reported with the corresponding 0–0 transition energy set to 0. The assignment of the most intense vibronic bands is also given. The computed spectrum has been simulated by convoluting the stick spectrum with Gaussian functions with HWHM of 10 cm^{-1}.

experimental bands are well reproduced without invoking overtone transitions, as needed in previous qualitative interpretations [108].

Although other pieces of information are available for this system, e.g. resonance Raman spectrum, together with IR, Raman, and UV–vis in different solvents, the selection of spectra described in this section together with those selected in the two previous ones is surely sufficient to point out the plethora of possibilities offered by the VMS tool. In the following section, the potentialities

of VMS in the field of magnetic spectroscopies are shown by means of an illustrative case.

1.4.4 EPR Spectrum in Different Solvents: The TOAC Case Study

Nitroxides (i.e. aminoxyl radicals) are among the most studied open-shell systems due to their remarkable stability coupled to strong localization of the unpaired electron on the NO moiety, which is, however, tuned by stereo-electronic and environmental effects. Thanks to remarkable technological and interpretative developments in EPR and ENDOR spectroscopy, nitroxides are more and more employed as spin labels and spin probes for the characterization of structural and dynamic properties of biomolecules and of nanostructures, together with their interactions with small molecules like dyes or drugs.

The main pieces of information provided by high-field EPR spectroscopy include nitrogen hyperfine (**A**) and gyromagnetic (**g**) tensors (which are local in nature) together with spin coupling **J** and dipolar spin–spin (**T**) interactions whenever two radical species are present even at not too short (7–10 Å) distances. However, the interpretation of experimental spectra in terms of structural characteristics and dynamical modulation effects strongly benefits from reliable computational simulations. The theoretical tools needed by EPR spectroscopists are provided by quantum chemistry for the prediction of the spin Hamiltonian parameters and by molecular dynamics and statistical mechanics for spectral line shapes. As mentioned above, the VMS software includes an integrated model that is the combination of (i) QC calculations of structural parameters and magnetic tensors, possibly including average interactions with the environment (by discrete–continuum models) and short-time dynamical effects; (ii) direct feeding of the calculated molecular parameters into dynamic models based on molecular dynamics and coarse-grained dynamics; and (iii) stochastic modeling based on the SLE. A fine-tuning of a limited set of molecular or mesoscopic parameters via a fitting procedure can be also performed if required.

The QC computation of magnetic tensors has a long history and has been revolutionized by hybrid density functionals coupled to purposely tailored basis sets describing in a sufficiently flexible way both the nuclear cusp and CV regions. In particular, the PBE0/SNSD model performs particularly well for the evaluation of hyperfine and gyromagnetic tensors. As an example, the experimental isotropic hyperfine coupling of the TEMPO radical (Figure 1.19) is about 15 G, and the value obtained at the PBE0/SNSD level is 14.95. Solvent effects on this parameter can be traced back to the increased contribution of the ionic resonance form (b) of Figure 1.19, which increases the solvent polarity. Taking bulk solvent effects into account by means of the polarizable continuum model (PCM) [111] leads to a remarkable agreement between theory and experiment: in a cyclohexane solution, the comparison is 15.28 vs. 15.26 G, and in toluene, 15.40 vs. 15.32 G. However, the same model leads to a much worse agreement for aqueous solutions (16.91 vs. 15.87 G). In this case, the explicit consideration of the pair of water molecules strongly interacting (via hydrogen bonds) with the oxygen atom leads to a computed value of 16.52 G, in remarkable agreement with experiment.

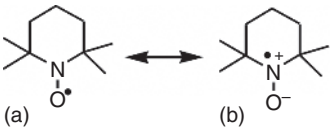

Figure 1.19 Resonance forms of the TEMPO radical.

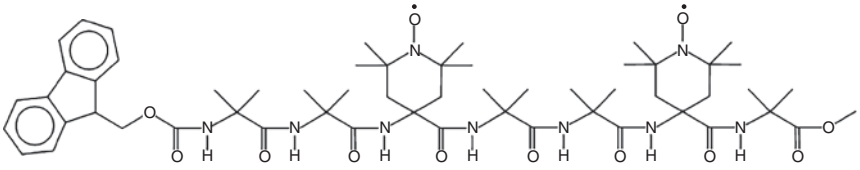

Figure 1.20 Fmoc-(Aib-Aib-TOAC)$_2$-Aib-OMe.

On these grounds, one can confidently employ in the integrated approach sketched above magnetic tensors computed at the PBE0/SNSD level, which is a model affordable also for quite large models of biomolecules. As an example, let us discuss in some detail the case of the double-spin-labeled, terminally protected heptapeptide Fmoc-(Aib-Aib-TOAC)$_2$-Aib-OMe (see Figure 1.20) in different solvents and at different temperatures (Fmoc, fluorenyl-9-methoxycarbonyl; Aib, α-aminoisobutyric acid; TOAC, 2,2,6,6-tetramethylpiperidine-1-oxyl-4-amino-4-carboxylic acid; OMe, methoxy). This molecule is characterized by the presence of two TOAC nitroxide free radicals (at relative positions [i, i+3]), which together with Aib represent two of the strongest helicogenic $C^{\alpha,\alpha}$-tetrasubstituted, α-amino acids. The 3_{10}-helix structure experimentally determined by X-ray diffractometric analysis in the solid state was well reproduced by PBE0/SNSD geometry optimizations *in vacuo*. On these grounds, a new force field was parameterized for both Aib and TOAC based on extensive QC computations [112, 113]. Two regular structures (namely, α-helix and 3_{10} helix) correspond to the energy minima for the heptapeptide *in vacuo*. In particular, the 3_{10} helix is more stable by about 3 kcal mol^{-1}, but polar solvents stabilize preferentially the α-helix, so that both species should be present, with solvent-dependent relative percentages. This is particularly significant since the computed EPR spectra of the two limiting structures are remarkably different. Several molecular dynamics simulations in different solvents were performed with the new force field, which, in turn, provided the structures (corresponding to a large number of statistically independent snapshots) for the QC evaluation of relative stabilities and magnetic tensors. By following the general strategy described in Section 1.3.4, determining the CW EPR spectrum of this biradical is relatively straightforward using the VMS software. As a first step, the spectra of the peptide in acetonitrile in the temperature range of 270–330 K were simulated and compared. A limited adjustment of the trace of the hyperfine tensor **A** (0.3 G to be compared with the estimated uncertainty of 0.5 G) leads to a remarkable agreement with experiment, which slightly worsens only at the lowest temperature (270 K). The agreement between experiment and spectra simulations performed considering the whole molecule as a simple Brownian rotor confirms that the molecular structure is essentially rigid in solution. However, solvents with different polarity can lead to the concomitant presence of both helical structures, thus issuing

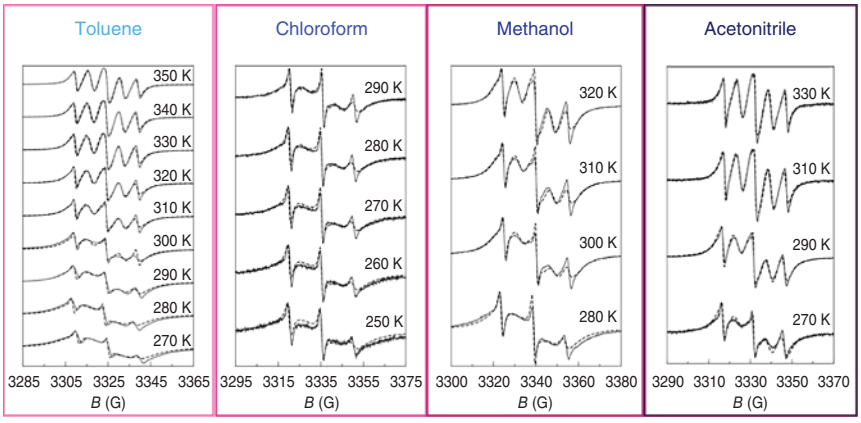

Figure 1.21 EPR spectra of Fmoc-(Aib-Aib-TOAC)$_2$-Aib-OMe in different solvents: solid lines represent experimental spectra, while dashed lines represent the simulated spectra.

strong modifications in the spectrum. If, for different solvents (acetonitrile, methanol, toluene, and chloroform), the relative percentages of 3_{10} helix and α-helix obtained from QC computations are used, a remarkable agreement between experiment and spectra simulations is noted (see Figure 1.21). This permits one to follow the transition from a fully 3_{10} helix to a fully α-helix structure when increasing the solvent polarity and the H-bond ability. Thus stereo-electronic, environmental, and dynamic effects can be properly analyzed and related to specific spectral features without any unbiased fitting and/or inference.

1.5 Conclusions

The identification and analysis of suitable molecular fingerprints in different regions of the electromagnetic spectrum have a deep impact in many research fields, ranging from astrochemistry, which aims at identifying molecular species in the interstellar medium, to the *in silico* design of multifunctional materials, just to provide a couple of examples. However, reliable computational simulations of the spectroscopic properties for complex systems require the integration of computational protocols that describe nonperiodic systems over length scales of 10^{-8} m and capture molecular motions and supramolecular interactions over several time scales. This task cannot always be accomplished by computing a few parameters for an isolated system, but instead it requires the integration of several paradigms and hence the application of many different algorithms. While this integration may be straightforwardly pursued in research groups specialized in computational chemistry, it involves a number of difficulties for experimentally oriented researchers. It is in view of overcoming such a gap that the VMS project was born and it is still in progress. Indeed, the development and exploitation of sophisticated virtual laboratories and computational chemistry cyberinfrastructures, in which data- and compute-centric resources coexist, can

represent an effective solution to overcome this limitation and increase the space and time scales of problems that can be tackled by computational modeling.

Advanced cyberinfrastructures allow a nearly real-time analysis via modern algorithms at multiple scales without requiring an in-depth computational background; therefore, scientists can effortlessly use HPC computational and data resources thanks to recent developments in hardware and software environments. In the framework of a general virtual platform, we have described in this chapter the VMS software, which integrates powerful computational approaches for several spectroscopies, thus spanning a large part of the electromagnetic field, with a general GUI, which takes care of both graphical input and output analysis, also in terms of a direct comparison with experimental spectra.

Acknowledgments

All the present and past members of the SMART center (http://dreams.sns.it) are acknowledged for their contributions to the ongoing development of the VMS tool. A special thanks to Dr. Daniele Licari and Dr. Lorenzo Spada for their help in preparing some figures.

References

1 Laane, J. (2018). *Frontiers and Advances in Molecular Spectroscopy*. Elsevier B.V.
2 Berova, N., Polavarapu, P., Nakanishi, K., and Woody, R.W. (eds.) (2012). *Comprehensive Chiroptical Spectroscopy: Instrumentation, Methodologies, and Theoretical Simulations*. Hoboken, NJ: Wiley.
3 Stephens, P., Devlin, F.J., and Cheeseman, J.R. (2012). *VCD Spectroscopy for Organic Chemists*. Boca Raton, FL: CRC Press and Taylor & Francis Group.
4 Zerbetto, M., Licari, D., Barone, V., and Polimeno, A. (2013). *Mol. Phys.* 111: 2746–2756.
5 Jensen, P. and Bunker, P.R. (2000). *Computational Molecular Spectroscopy*. Chichester: Wiley.
6 Barone, V. (2011). *Computational Strategies for Spectroscopy: From Small Molecules to Nano Systems*. Wiley.
7 Barone, V. (2016). *WIREs Comput. Mol. Sci.* 6: 86–110.
8 Barone, V., Baiardi, A., Biczysko, M. et al. (2012). *Phys. Chem. Chem. Phys.* 14: 12404–12422.
9 Barone, V., Baiardi, A., and Bloino, J. (2014). *Chirality* 26: 588–600.
10 Licari, D., Tasinato, N., Spada, L. et al. (2017). *J. Chem. Theory Comput.* 13: 4382–4396.
11 Presti, D., Pedone, A., Licari, D., and Barone, V. (2017). *J. Chem. Theory Comput.* 13: 2215–2229.
12 Licari, D., Baiardi, A., Biczysko, M. et al. (2015). *J. Comput. Chem.* 36: 321–334.

13 Bloino, J., Biczysko, M., and Barone, V. (2015). *J. Phys. Chem. A* 119: 11862–11874.
14 Frisch, M.J., Trucks, G.W., Schlegel, H.B. et al. (2016). *Gaussian 16 Revision A.03*. Wallingford, CT: Gaussian Inc.
15 Stanton, J.F., Gauss, J., Harding, M.E., and Szalay, P.G. (2016). CFour A quantum chemical program package", with contributions from A.A. Auer, R.J. Bartlett, U. Benedikt et al. Watts and the integral packages MOLECULE (J. Almlof and P.R. Taylor), PROPS (P.R. Taylor), ABACUS (T. Helgaker, H.J.Aa. Jensen, P. Jorgensen, and J. Olsen), and ECP routines by A.V. Mitin and C. van Wüllen. For the current version, see http://www.cfour.de (accessed 2018).
16 Aliev, M.R. and Watson, J.K.G. (1985). High-order effects on the vibration-rotation spectra of semirigid molecules. In: *Molecular Spectroscopy: Modern Research*, vol. 3, Chapter 1 (ed. K.N. Rao). Academic Press 1–67.
17 Watson, J.K.G. (1968). *J. Chem. Phys.* 48: 4517–4524.
18 Mills, I.M. (1972). Vibration-rotation structure in asymmetric- and symmetric-top molecules. In: *Molecular Spectroscopy: Modern Research* (ed. K.N. Rao and C.W. Mathews). New York: Academic Press 115–140.
19 Watson, J.K.G. (1977). Aspects of quartic and sextic centrifugal effects on rotational energy levels. In: *Vibrational Spectra and Structure, A Series of Advances*, vol. 6 (ed. J. Durig). Amsterdam, Netherlands: Elsevier 1–89.
20 Nielsen, H.H. (1951). *Rev. Mod. Phys.* 23: 90–136.
21 Willets, A., Handy, N.C., Green, W.H. Jr., and Jayatilaka, D. (1990). *J. Phys. Chem.* 94: 5608–5616.
22 Vázquez, J. and Stanton, J.F. (2006). *Mol. Phys.* 104: 377–388.
23 Vázquez, J. and Stanton, J.F. (2007). *Mol. Phys.* 105: 101–109.
24 Bloino, J. and Barone, V. (2012). *J. Chem. Phys.* 136: 124108.
25 Bloino, J. (2015). *J. Phys. Chem. A* 119: 5269–5287.
26 Amos, R.D., Handy, N.C., Green, W.H. et al. (1991). *J. Chem. Phys.* 95: 8323–8336.
27 Bouř, P. (1994). *J. Phys. Chem.* 98: 8862–8865.
28 Martin, J.M.L., Lee, T.J., Taylor, P.M., and François, J.-P. (1995). *J. Chem. Phys.* 103: 2589–2602.
29 Kuhler, K.M., Truhlar, D.G., and Isaacson, A.D. (1996). *J. Chem. Phys.* 104: 4664–4670.
30 Martin, J.M.L. and Taylor, P.M. (1997). *Spectrochim. Acta, Part A* 53: 1039–1050.
31 Miani, A., Cané, E., Palmieri, P. et al. (2000). *J. Chem. Phys.* 112: 248–259.
32 Hänninen, V. and Halonen, L. (2003). *Mol. Phys.* 101: 2907–2916.
33 Barone, V. (2005). *J. Chem. Phys.* 122: 014108.
34 Begue, D., Carbonniere, P., and Pouchan, C. (2005). *J. Phys. Chem. A* 109: 4611–4616.
35 Cané, E., Miani, A., and Trombetti, A. (2007). *J. Phys. Chem. A* 111: 8218–8222.
36 Matthews, D.A. and Stanton, J.F. (2009). *Mol. Phys.* 107: 213–222.
37 Bloino, J., Biczysko, M., and Barone, V. (2012). *J. Chem. Theory Comput.* 8: 1015–1036.

38 Hermes, M.R. and Hirata, S. (2013). *J. Chem. Phys.* 139: 034111.
39 Krasnoshchekov, S.V., Isayeva, E.V., and Stepanov, N.F. (2014). *J. Chem. Phys.* 141: 234114.
40 Piccardo, M., Bloino, J., and Barone, V. (2015). *Int. J. Quantum Chem.* 115: 948–982.
41 Darling, B.T. and Dennison, D.M. (1940). *Phys. Rev.* 57: 128–139.
42 Lehmann, K.K. (1989). *Mol. Phys.* 66: 1129–1137.
43 Matthews, D.A., Vázquez, J., and Stanton, J.F. (2007). *Mol. Phys.* 105: 2659–2666.
44 Krasnoshchekov, S.V., Isayeva, E.V., and Stepanov, N.F. (2012). *J. Phys. Chem. A* 116: 3691–3709.
45 Rosnik, A.M. and Polik, W.F. (2014). *Mol. Phys.* 112: 261–300.
46 Bloino, J., Baiardi, A., and Biczysko, M. (2016). *Int. J. Quantum Chem.* 116: 1543–1574.
47 Bloino, J., Biczysko, M., Santoro, F., and Barone, V. (2010). *J. Chem. Theory Comput.* 6: 1256–1274.
48 Baiardi, A., Bloino, J., and Barone, V. (2013). *J. Chem. Theory Comput.* 9: 4097–4115.
49 Egidi, F., Fusé, M., Baiardi, A. et al. (2018). *Chirality* 30: 850–865.
50 Franck, J. (1926). *Trans. Faraday Soc.* 21: 536–542.
51 Condon, E.U. (1928). *Phys. Rev.* 32: 858–872.
52 Herzberg, G. and Teller, E. (1933). *Z. Phys. Chem. Abt. B* 21: 410–446.
53 Dushinsky, F. (1937). *Acta Phys. URSS* 7: 551.
54 Baiardi, A., Bloino, J., and Barone, V. (2016). *J. Chem. Phys.* 144: 084114.
55 Baiardi, A., Bloino, J., and Barone, V. (2017). *J. Chem. Theory Comput.* 13: 2804–2822.
56 Cimino, P., Neese, F., and Barone, V. (2010). Calculation of magnetic tensors and EPR spectra for free radicals in different environments. In: *Computational Spectroscopy: Methods, Experiments and Applications* (ed. J. Grununberg). Wiley-VCH 1000–1030.
57 Polimeno, A., Barone, V., and Freed, J.H. (2011). Stochastic methods for magnetic resonance spectroscopies. In: *Computational Strategies for Spectroscopy, from Small Molecules to Nano Systems* (ed. V. Barone). Chichester: Wiley 549–582.
58 Harriman, J.E. and Loebl, E.M. (2013). *Theoretical Foundations of Electron Spin Resonance*. Elsevier Science.
59 Improta, R. and Barone, V. (2004). *Chem. Rev.* 104: 1231–1254.
60 Fermi, E. (1930). *Z. Phys.* 60: 320.
61 Frosch, A. and Foley, H.M. (1952). *Phys. Rev.* 88: 1337.
62 Barone, V. and Cimino, P. (2009). *J. Chem. Theory Comput.* 5: 192–199.
63 Barone, V., Biczysko, M., Bloino, J. et al. (2013). *J. Chem. Phys.* 138: 234303.
64 Heckert, M., Kállay, M., and Gauss, J. (2005). *Mol. Phys.* 103: 2109.
65 Heckert, M., Kállay, M., Tew, D.P. et al. (2006). *J. Chem. Phys.* 125: 044108.
66 Puzzarini, C. and Barone, V. (2011). *Phys. Chem. Chem. Phys.* 13: 7189–7197.
67 Barone, V., Biczysko, M., Bloino, J., and Puzzarini, C. (2013). *Phys. Chem. Chem. Phys.* 15: 10094–10111.

68 Tajti, A., Szalay, P.G., Császár, A.G. et al. (2004). *J. Chem. Phys.* 121: 11599–11613.

69 Mendolicchio, M., Penocchio, E., Licari, D. et al. (2017). *J. Chem. Theory Comput.* 13: 3060–3075.

70 Raghavachari, K., Trucks, G.W., Pople, J.A., and Head-Gordon, M. (1989). *Chem. Phys. Lett.* 157: 479–483.

71 Puzzarini, C., Stanton, J.F., and Gauss, J. (2010). *Int. Rev. Phys. Chem.* 29: 273–367.

72 Grimme, S. (2006). *J. Chem. Phys.* 124: 034108.

73 Penocchio, E., Piccardo, M., and Barone, V. (2015). *J. Chem. Theory Comput.* 11: 4689–4707.

74 Biczysko, M., Panek, P., Scalmani, G. et al. (2010). *J. Chem. Theory Comput.* 6: 2115–2125.

75 Puzzarini, C., Biczysko, M., and Barone, V. (2010). *J. Chem. Theory Comput.* 6: 828–838.

76 Puzzarini, C., Biczysko, M., and Barone, V. (2011). *J. Chem. Theory Comput.* 7: 3702–3710.

77 Becke, A.D. (1993). *J. Chem. Phys.* 98: 5648–5652.

78 Lee, C., Yang, W., and Parr, R. (1988). *Phys. Rev. B* 37: 785–789.

79 Møller, C. and Plesset, M.S. (1934). *Phys. Rev.* 46: 618–622.

80 Fau, S. and Bartlett, R.J. (2003). *J. Phys. Chem. A* 107: 6648.

81 Barone, V. (1995). *Recent Advances in Density Functional Methods*. Singapore: World Scientific.

82 Puzzarini, C. and Barone, V. (2010). *J. Chem. Phys.* 133: 184301.

83 Lipparini, F. and Barone, V. (2011). *J. Chem. Theory Comput.* 7: 3711–3724.

84 Lipparini, F., Cappelli, C., and Barone, V. (2012). *J. Chem. Theory Comput.* 8: 4153–4165.

85 Carnimeo, I., Cappelli, C., and Barone, V. (2015). *J. Comput. Chem.* 31: 2271–2290.

86 Lipparini, F., Cappelli, C., Scalmani, G. et al. (2012). *J. Chem. Theory Comput.* 8: 4270–4278.

87 Giovannini, T., Olszowka, M., Egidi, F. et al. (2017). *J. Chem. Theory Comput.* 13: 4421–4435.

88 Pickett, H.M. (1991). *J. Mol. Spectrosc.* 148: 371–377.

89 Loru, D., Bermudez, M.A., and Sanz, M. (2016). *J. Chem. Phys.* 145: 074311.

90 Pulay, P., Meyer, W., and Boggs, J.E. (1978). *J. Chem. Phys.* 68: 5077–5085.

91 Demaison, J., Boggs, J.E., and Császár, A.G. (2010). *Equilibrium Molecular Structures: From Spectroscopy to Quantum Chemistry*. CRC Press.

92 Piccardo, M., Penocchio, E., Puzzarini, C. et al. (2015). *J. Phys. Chem. A* 119: 2058–2082.

93 Pawlowski, F., Jørgensen, P., Olsen, J. et al. (2002). *J. Chem. Phys.* 116: 6482–6496.

94 Bartell, L.S., Romenesko, D.J., and Wong, T.C. (1975). *Molecular Structure by Diffraction Methods*, vol. 3. Cambridge: Royal Society of Chemistry.

95 Colarusso, P., Zhang, K.Q., Guo, B., and Bernath, P.F. (1997). *Chem. Phys. Lett.* 269: 39–48.

96 Grimme, S., Ehrlich, S., and Goerigk, L. (2011). *J. Comput. Chem.* 32: 1456–1465.

97 Császár, A.G., Allen, W.D., and Schaefer, H.F. III (1998). *J. Chem. Phys.* 108: 9751.

98 Barone, V. and Polimeno, A. (2006). *Phys. Chem. Chem. Phys.* 8: 4609–4629.

99 Puzzarini, C. and Barone, V. (2018). *Acc. Chem. Res.* 51: 548–556.

100 Barone, V., Biczysko, M., Bloino, J., and Puzzarini, C. (2013). *J. Chem. Theory Comput.* 9: 1533–1547.

101 Stepanian, S.G., Reva, I.D., Radchenko, E.D. et al. (1998). *J. Phys. Chem. A* 102: 1041–1054.

102 Carnimeo, I., Biczysko, M., Bloino, J., and Barone, V. (2011). *Phys. Chem. Chem. Phys.* 13: 16713–16727.

103 Barone, V., Biczysko, M., Bloino, J., and Puzzarini, C. (2014). *J. Chem. Phys.* 141: 034107.

104 Merten, C., Bloino, J., Barone, V., and Xu, Y. (2013). *J. Phys. Chem. Lett.* 4: 3424–3428.

105 Sebestik, J. and Bour, P. (2011). *J. Phys. Chem. Lett.* 2: 498–502.

106 Biczysko, M., Bloino, J., Brancato, G. et al. (2012). *Theor. Chem. Acc.* 131: 1–19.

107 Kisiel, Z., PszczóĺkowskI, L., Lopez, J.C. et al. (1999). *J. Mol. Spectrosc.* 195: 332.

108 da Silva, F.F., Almeida, D., Martins, G. et al. (2010). *Phys. Chem. Chem. Phys.* 12: 6717–6731.

109 Cacelli, I., Ferretti, A., Prampolini, G., and Barone, V. (2015). *J. Chem. Theory Comput.* 11: 2024–2035.

110 Lin, N., Santoro, F., Rizzo, A. et al. (2009). *J. Phys. Chem. A* 113: 4198–4207.

111 Mennucci, B. (2012). *WIREs Comput. Mol. Sci.* 2: 386–404.

112 Stendardo, E., Pedone, A., Cimino, P. et al. (2010). *Phys. Chem. Chem. Phys.* 12: 11697–11709.

113 Grubisic, S., Brancato, G., and Barone, V. (2013). *Phys. Chem. Chem. Phys.* 15: 17395–17407.